

Syracuse University

SURFACE at Syracuse University

Dissertations - ALL

SURFACE at Syracuse University

Summer 8-27-2021

Self-organization in Models of Cyclically Sheared Suspensions

Jikai Wang

Syracuse University

Follow this and additional works at: <https://surface.syr.edu/etd>



Part of the [Physics Commons](#)

Recommended Citation

Wang, Jikai, "Self-organization in Models of Cyclically Sheared Suspensions" (2021). *Dissertations - ALL*. 1356.

<https://surface.syr.edu/etd/1356>

This Dissertation is brought to you for free and open access by the SURFACE at Syracuse University at SURFACE at Syracuse University. It has been accepted for inclusion in Dissertations - ALL by an authorized administrator of SURFACE at Syracuse University. For more information, please contact surface@syr.edu.

Abstract

This thesis presents a study of random self-organized systems using computer simulated models inspired by cyclically-sheared non-Brownian suspensions of monodisperse spherical particles in a density-matched fluid. When driven at low Reynolds number, such systems have vanishing thermal fluctuations and only short-range interactions between individual particles. Nevertheless, they show intriguing collective behaviors at large length scales, such as a strong suppression of fluctuations in the number density. Such self-organized “hyperuniform” states can be useful in industrial applications where well-controlled states can ease the processing of such materials.

In Chapter 2, we propose a new way of generating hyperuniform suspensions, by incorporating slow gravity-driven sedimentation into a cyclically-sheared suspension. The effect of self-compaction drives the particle system towards its critical state automatically. We thus achieve quality hyperuniform distribution without fine-tuning of the system parameters. Computer simulations were conducted that mimic an experimental setup, and we successfully demonstrated a process leading to hyperuniformity in the steady state in the simulations. To this end, we characterize the spatial structure in both real space and reciprocal space to bolster our findings.

In Chapter 3, we were inspired by dynamical jamming fronts [1], which prompted us to conduct a detailed study of our sheared suspension system with sedimentation that shows a qualitatively similar propagating front. We conducted extensive measurements to better describe the compaction front in this dilute system that is far from jamming. We found that the density profile of the front is solely dependent

on geometric parameters of the system; its surprisingly does not vary with the effective diffusion rate. To further investigate the formation of the compaction front, we conducted point perturbation simulations to extract a correlation length in homogeneous systems as the critical packing fraction is approached from below. We show that the scaling exponent of the compaction front width compares favorably with the correlation length from our point perturbation measurements, and could be consistent with either the directed percolation universality class or conserved directed percolation.

In Chapter 4, we summarize this body of work and present an outlook for future directions.

Self-organization in models of cyclically sheared suspensions

by

Jikai Wang

B.S., University of Science and Technology of China, 2014

Dissertation

Submitted in partial fulfillment of the requirements for the degree of
Doctor of Philosophy in Physics.

Syracuse University
August 2021

Copyright © Jikai Wang 2021

All Rights Reserved

Acknowledgements

I would like to express my deepest appreciation to my advisors, Professor Joseph Paulsen and Professor Jennifer Schwarz. Joey and Jen guided me through my entire doctoral research and paper preparations. Their profound knowledge of physics and mathematics impressed me and set a high standard for me to pursue the truth and logic behind any real-world phenomenon with solid research. Their thoughtfulness and patience has helped me to have a smooth experience not only in academic research, but also in every-day life. Without their mentorship and support, I would not be able to complete my research and write up this thesis. I appreciate it a lot.

I would also like to extend my gratitude to all the PhD committee members including Teng Zhang, Jennifer Ross, Alison Patteson, and Liviu Movileanu, as well as Lisa Manning who served on my oral defense committee. I'm very grateful to them for taking the time and effort to go through my work and provide insightful questions towards my research.

I also thank Nathan Keim and Laurent Corté for enlightening discussions. They helped us clarify our work in Chapter 2 when it was being prepared for publication, which increased our confidence in our simulation results.

I am also grateful to all the help and support I received from my colleagues including Kuang Liu, Yebin Liu, Zhuoming Li, Monica Ripp, Yousra Timounay, Raj De, Zachariah Schrecengost, Mengfei He and Yuezhe Yao. I enjoy the time spending with them not only when doing research, but also when chatting which enriched my life over the past few years.

I would also like to thank my friend Dan Li, He Yan, Yao Xiao, Jeff Chen, Wei Wang, Bing Yang, Yini Li, Jun Yu and others who I spent a lot of time with and brought me cherishable memories over the years in Syracuse.

Finally, I'm deeply indebted to my parents for their unconditional support through my entire study and research period in the US. They've helped me not only emotionally but also financially, especially in my difficult times. I deeply appreciate that.

Lastly, I want to say that the most important thing I received from my Ph.D. study is the true happiness I perceived when discovering interesting little things that exist in the world around us. Nature has its beauty built in and, as observers, we should humble ourselves and only interact with it respectfully. The more you learn from it, the more you will feel this way.

“ We hold these truths to be sacred and undeniable; that all men are created equal and independent, that from that equal creation they derive rights inherent and inalienable, among which are the preservation of life, and liberty, and the pursuit of happiness. ”

Thomas Jefferson, *the Declaration of Independence*

Contents

Abstract	i
Acknowledgements	v
1 Introduction	1
1.1 Granular systems	2
1.1.1 Experiments on cyclically sheared suspensions	3
1.1.2 Universality Class of Random Organization	5
1.1.3 Previous simulations	6
1.2 Hyperuniformity	9
1.2.1 Hyperuniformity in nature	10
1.2.2 Hyperuniformity in suspensions	10
1.2.3 Hyperuniformity in other systems	12
1.3 Inhomogeneous systems	12
1.3.1 Driving disordered systems out of inhomogeneous states	12
1.3.2 Density fronts in driven particle systems	14
2 Hyperuniformity with no fine tuning in sheared sedimenting suspensions	19
2.1 Introduction	19
2.2 Model	21
2.2.1 Implementation	23
2.3 Self-organized criticality	23

2.3.1	Dependence of self-organized criticality on collision rule.	26
2.3.2	Structure factor	28
2.3.3	Density fluctuations in real space	30
2.3.4	Finite size effects	32
2.4	Loss of hyperuniform scaling by linear density gradients	32
2.4.1	Variance of density in a continuous system with a linear density gradient	34
2.4.2	Vertical density profile	36
2.4.3	Magnitude of vertical density gradient	37
2.4.4	Phase diagram	38
2.5	One-dimensional model	40
2.6	Discussion	41
3	Self-organized compaction fronts in cyclically-sheared sinking grains	49
3.1	Background	49
3.1.1	Dynamical jamming front	50
3.2	Sedimenting suspensions	51
3.2.1	Model	51
3.2.2	Front velocity and particle conservation	54
3.2.3	Derivation of the front profile	55
3.3	Correlation lengthscale	56
3.3.1	Point perturbation	57
3.4	Universality class	58
3.4.1	Calculation of scaling exponents	58
3.4.2	Compared with DP and CDP	59
3.5	Discussion	59

4 Conclusion	62
4.1 Summary	62
4.2 Future works	63
4.2.1 Hyperuniformity in higher dimension	63
4.2.2 Hyperuniformity in networks	64
4.2.3 Robustness of hyperuniform networks	64
Bibliography	65
Vita	75

List of Figures

1.1	[2] (left) Simulated packing of particles with the color scheme denoting the number of contacts per particle. [3] (right) A cross-section of micron-sized colloidal particles in suspension.	1
1.2	Experimental setup used to study self-organization under cyclic shear by Ref. [31]. (a) Setup where two concentric cylinders are used to shear the sample in the gap between them. A laser sheet projected from the side allows a two-dimensional slice to be seen. (b) Image of the suspension. (c) Difference of particle images between two shearing cycles in a reversible state. The image is monotone indicating reversible particle trajectories. (d) Difference of particle images between two shearing cycles in an irreversible state, where light and dark regions are from the net particle displacements.	4
1.3	Simulation model by [30]. This schematic illustrates the shearing process in a 2D simulation model proposed by Corté to mimic the corresponding experimental setup. After calculating the particle displacements under an affine transformation, one then checks for collisions and marks those particles to be given random kicks before the next cycle.	9
1.4	[38] Top Patterns of avian photoreceptors in a chicken’s eye. Bottom Structural factors of corresponding color cells.	11

1.5	[40] Top An example of stealthy scalar field Bottom The measured structural factor over different wavelength plotted in log-scale. A hollow central area indicates reduced fluctuations over the long range.	16
1.6	Sheared sedimenting suspensions in experiments by Corté <i>et al.</i> (a) Experimental setup from Ref. [39] for the sheared suspension system with sedimentation. (b) Image of the suspension showing a two-dimensional slice illuminated with a laser sheet.	17
1.7	Illustration of the corresponding simulations from Ref. [39]. Solid particles are packed loosely in a 2D system while being sheared and sedimenting. Red particles are those who encountered other particles during shearing which will be given random kicks.	17
1.8	Dynamical jamming front in a two-dimensional model experiment, reproduced from Ref. [44]. The image sequence, from top to bottom, shows the evolution of an unjammed system being pushed from one side. A propagating density front can be seen that separates the area of initial packing and the area of jammed packing.	18

2.1 **Sheared non-Brownian suspension model after Ref. [30].** **(a)** Phase diagram showing reversible steady states at low volume fraction, ϕ and strain amplitude, γ . Outside this region, a finite fraction of particles collides during each cycle in the steady state. Dashed line: Critical phase boundary. Data show the largest γ where we obtain a reversible state in simulations with $N = 10186$ particles. **(b)** Simulation algorithm. In each shear cycle, particles are displaced a horizontal distance $\Delta x = \gamma y$ and then returned to their initial positions. Particles that overlap (red) are given random kicks, to simulate local irreversibility due to collisions. **(c)** Interaction region around a particle. A second particle with its center anywhere inside the dashed circle will overlap with the particle at the origin (shown as a dark circle); they would both receive a random kick. Shearing the system expands the interaction region to the entire shaded area (shown for one value of γ), which contains the points that are covered by continuously shearing the dashed circle up to strain amplitude γ and back.

..... 22

- 2.2 Self-organized criticality at low sedimentation speed.** (a) Snapshot of system in steady state. Red particles are colliding in the current cycle. (b) Area fraction (plotted on the x axis) versus vertical coordinate, y , at low and high sedimentation velocity v_s , with $N = 2547$, $\gamma = 3.0$, $\kappa = 25.5$, and $L = 100$. Vertical dashed line shows $\phi_c(\gamma = 3) = 0.20$. (c) Scaled steady-state volume fraction ϕ_∞/ϕ_c , measured over a wide range of system parameters (κ , γ , and N as shown in legend) and velocities ($10^{-5} < v_s < 10^{-2}$). *Inset*: Measurements versus the parameter $A = (\pi/\phi_c)^{3/2}d^3\kappa^2v_s/32D$, proposed by Ref. [39]. The data is not collapsed. *Main*: The data collapse when re-plotted versus \bar{A} (Eq. 2.1). For $\bar{A} \ll 1$ (low sedimentation speed), the steady-state volume fraction ϕ_∞ is equal to the critical value ϕ_c . Error bars are from fluctuations in system height in the steady state. 25
- 2.3 Results for multiple kicks.** Scaled steady-state density in a suspension sedimenting at velocity $10^{-4} < v < 10^{-1}$, sheared at strain amplitude γ . We use $N = 1000$, $\epsilon = 0.5$, and $1.6 < \kappa < 31.9$. The diffusion constant D is set to 0.0414, the value obtained by Corté *et al.* [39]. (a) The data only approximately collapse with $A = (\pi/\phi_c)^{3/2}d^3\kappa^2v_s/32D$, the scaling proposed by [39]. (b) The data collapse when plotted versus $\bar{A} = \pi d^2\kappa v_s/16\phi_c D$ 27

2.4 **Static structure factor.** $S(\mathbf{k})$ measured in 2D simulations with $N = 4827$, $\kappa = 34.1$, and $\epsilon = 0.5$, at three values of \bar{A} and in the steady state. Values are calculated using Eq. 2.2 at wavevectors k_x and k_y where an integer number of wavelengths fill the region populated by the particles. The sum is performed over the bottom 99% of the particles to avoid the diffuse boundary layer at the top of the sample. **(a)** Results for $\gamma = 0.5$. At low \bar{A} , a region with low intensity develops near the origin, signaling hyperuniformity. (This region is not circular because of the anisotropic driving.) **(b)** Results for $\gamma = 3$. Despite larger anisotropy in the structure, hyperuniformity occurs at low \bar{A} .

29

2.5 Number density fluctuations. **(a)** Steady-state variance of the number density, σ_ρ^2 , versus window size, ℓ , in 2D simulations with sedimentation and shear. The variance is calculated by measuring the number density of particle centers, ρ , in circular windows of diameter ℓ sampled uniformly throughout the suspension. Each curve is an average of 50 systems with $N = 9677$, $\gamma = 3.0$, and $\kappa = 48.4$. At low sedimentation speed, hyperuniform density fluctuations are observed, as shown by the dotted line following $0.17\ell^{-2.60}$. The data are also consistent with a larger exponent with a logarithmic correction: $\ell^{-3} \log(\ell)$ (solid line). An uncorrelated system would follow a scaling of ℓ^{-2} . **(b)** Analogous results in 1D simulations, averaged over 20 systems with $N = 3000$ and $\gamma = 1$. At low sedimentation speed, hyperuniform density fluctuations are observed over 3 decades in ℓ , following $0.15\ell^{-1.44}$. An uncorrelated system would follow a scaling of ℓ^{-1} . **(c)** Variance of the number density for initially hyperuniform 2D systems that were scaled along the y axis to impose a constant density gradient, $|\partial\phi/\partial y|$. Each curve is an average over 31 systems with $N = 10186$, $\gamma = 3.01$, $L = 200$, and $\phi = 0.2$. The variance increases with the size of the gradient. The data are precisely captured by summing the measurement at zero gradient with a term due to a uniform gradient that we calculate in the continuum limit (dashed lines: Eq. ?? computed with the value of $|\partial\phi/\partial y|$ in the legend). . . . 43

- 2.6 **Effect of system size on variance of the number density.** *Inset:* Variance of the number density, σ_ρ^2 , versus ℓ for a square system of size $L = 200$ and subsystems of size $L' < L$. The largest system has $N = 10186$, $\phi = 0.2$, and is sheared cyclically at amplitude $\gamma = 3.01 \approx \gamma_c$ until it reaches a reversible state. We thus obtain a hyperuniform configuration with a scaling exponent $\lambda = 2.60$. *Main:* We shift the curves by scaling the x axis by L/L' and y axis by $(L/L')^\lambda$. The data collapse onto a single master curve, which falls off rapidly when ℓL . 44
- 2.7 **Mapping a constant-density profile to a profile with a constant vertical gradient.** *Left:* Density profile, $\phi_L(y)$, versus vertical position, y (where the dependent variable is on the x axis so that vertical axis is oriented as in the simulation). The system has a uniform distribution along the y axis with a constant area fraction ϕ_0 . *Right:* Target density profile of the form $\phi_R(y) = ay + b$. The shaded region at position y with thickness dy is mapped to position y' with thickness dy' that conserves its mass. 44
- 2.8 **Calculation of variance in system with constant vertical density gradient** A box of height H and width L contains a continuous density field $\phi(y)$. The system has a constant vertical density gradient $\partial\phi/\partial y$ and densities ϕ_t and ϕ_b at the top and bottom boundaries, respectively. The variance of the number density $\sigma_\rho^2(\ell)$ is calculated by measuring the mean density in circular regions of diameter ℓ , sampled uniformly throughout the region. 45

2.9	Steady-state vertical density gradient.	$ \Delta\phi/\Delta y $ versus $d^2\kappa v_s^2/D^2$ (main) and versus \bar{A} (inset). Data are from fitting the density profile of the middle 60% of the particles, averaging over 5 systems for each point. Dashed line: Scaling argument with fitted numerical prefactor, Eq. 2.17.	46
2.10	Self-organized hyperuniformity.	(a) Variance of the number density, σ_ρ^2 , for sampling windows of size $\ell = 10$. The data over a wide range of parameters are collapsed when plotted versus $\bar{A}\sqrt{\phi_c}$. At low velocity (i.e., low $\bar{A}\sqrt{\phi_c}$), the data plateau to the value in the critical state. The increase at moderate velocities is well captured by Eq. 2.18 (dashed line) for the effect of vertical density gradients. (b) Magnitude of the local scaling exponent, λ , measured at $\ell = 10$. Hyperuniform scaling ($\lambda > 2$) is observed for $\bar{A}\sqrt{\phi_c} > 0.08$ at this lengthscale. (c) Phase diagram for hyperuniform density fluctuations. Hyperuniformity emerges below a finite threshold value of $\bar{A}\sqrt{\phi_c}$, and it extends to longer lengthscales as the control parameter $\bar{A}\sqrt{\phi_c}$ decreases. Symbols: Lengthscale ℓ_H where the local scaling exponent λ of the variance $\sigma_\rho^2(\ell)$ is shallower than 2. Dashed line: Phase boundary from our theory with no free parameters, Eq. 2.19.	47

2.11 One-dimensional model results. **(a)** Magnitude of the vertical density gradient, $|\Delta\phi/\Delta y|$ versus dNv_s^2/D^2 , in the steady state. Data are from fits to the middle 60% of the density profile, averaged over 20 systems. Dashed line: Predicted scaling, Eq. 2.21. **(b)** Phase diagram. Symbols: Lengthscale ℓ_H where the local scaling exponent λ of the variance $\sigma_\rho^2(\ell)$ is shallower than 1. As in our 2D systems, we measure the variance over the bottom 99% of particles, and we consider windows of size $\ell < h_\infty/5$ to avoid system size effects. Dashed line: Phase boundary from our theory with no free parameters, Eq. 2.23. As in 2D, hyperuniform scaling emerges below a finite threshold value of $\bar{A}\sqrt{\phi_c}$ and extends to longer lengthscales at smaller $\bar{A}\sqrt{\phi_c}$ 48

3.1 Self-organized compaction front. **(a)** Simplified model of a cyclically-sheared suspension after Ref. [30]. In each cycle, a uniform sedimentation velocity v_s is applied to all particles, and particles that overlap (red) are given random kicks, to simulate local irreversibility due to collisions. **(b)** In the simulations, a dense region grows upwards with a front velocity v_f . When the front reaches the top of the system, a steady state is attained. **(c)** Scaled front velocity, v_f/v_s . Dashed line: Theoretical prediction [Eq. (3.1)], which assumes that the dilute and dense phases have uniform densities equal to ϕ_0 and ϕ_c (measured independently). Parameter ranges: $0.05 \leq \epsilon \leq 10$, $300 < N < 16300$, $10^{-6} \leq v_s \leq 4 \times 10^{-4}$, $0.05 \leq \phi_0 \leq 0.40$, $0.15 \leq \phi_c \leq 0.44$ 52

3.2 Interface shape and thickness. (a) Density profile snapshots, spaced evenly in time. The system has $\epsilon = 0.5$, $v_s = 1.7 \times 10^{-5}$, $\phi_0 = 0.2$, $\phi_c = 0.376$. Translating these 6 profiles atop one another shows that the front propagates with a fixed shape and width. The measured profile is consistent with a sigmoid function (dashed line). We fit this function to the data to measure the front width, Δ_f , for each simulation. **(c)** Measured front width, Δ_f , versus distance to criticality of the sedimenting phase, $\phi_c - \phi_0$. Closed symbols: transient fronts. Open symbols: interface at the top of the system in the steady state (where ϕ_0 is therefore taken to be zero). The data at sufficiently small $\phi_c - \phi_0$ are consistent with a power-law with exponent -1.20 ± 0.15 (dashed line). **(d,e)** To test for any dependence on other system parameters, we divide the data by the power-law fit in panel (c). The behavior shows no trend with kick size, ϵ . There is also no growth of the front width with the system width, which would occur if the interface were rough. Parameter ranges in (c-e): $0.05 \leq \epsilon \leq 10$, $300 < N < 8600$, $10^{-7} \leq v_s \leq 4 \times 10^{-4}$, $0.05 \leq \phi_0 \leq 0.40$, $0.15 \leq \phi_c \leq 0.44$ 53

3.3 **Response to point perturbation.** **(a)** Starting from a quiescent state, a perturbation may set off a chain reaction in which many particles are activated before the system becomes quiescent again. The red particles were active at some time during the avalanche; darker particles received more total kicks. **(b)** Histograms collected over many systems for the distance to the farthest activated particle, ℓ , the number of activated particles, n , and the avalanche duration in cycles, t . Solid lines: Fits to Eq. (3.7), where the measured exponent α is indicated in each panel. **(c)** The curves are approximately collapsed when scaled by the position of the exponential cutoff. **(d)** Value of the cutoff versus $\phi_c - \phi_0$. Each curve diverges as a power law, with another exponent that is distinct from α (see Table 3.1). All data are for $\epsilon = 0.5$ and $L = 400$

List of Tables

3.1 **Comparison of critical exponents.** Values are shown for directed percolation (DP, obtained from Ref. [34]), conserved directed percolation (CDP/Manna, obtained from Ref. [35]) and the present work using point perturbations in the isotropic random organization model. Greek notation matches that of Ref. [34]. 57

Chapter 1

Introduction

This dissertation focuses on the self-organization of disordered systems using computer simulations and statistical analysis techniques. A particularly simple disordered system might be a collection of random discs in a plane, perhaps produced from a stochastic process without any external stress or any long-range interactions. Such a system does not have any obvious correlations or discrete symmetries and no obvious order can be found in it. Other systems that appear random upon first glance may reveal more subtle order on further analysis; we will visit specific examples of this in my work.

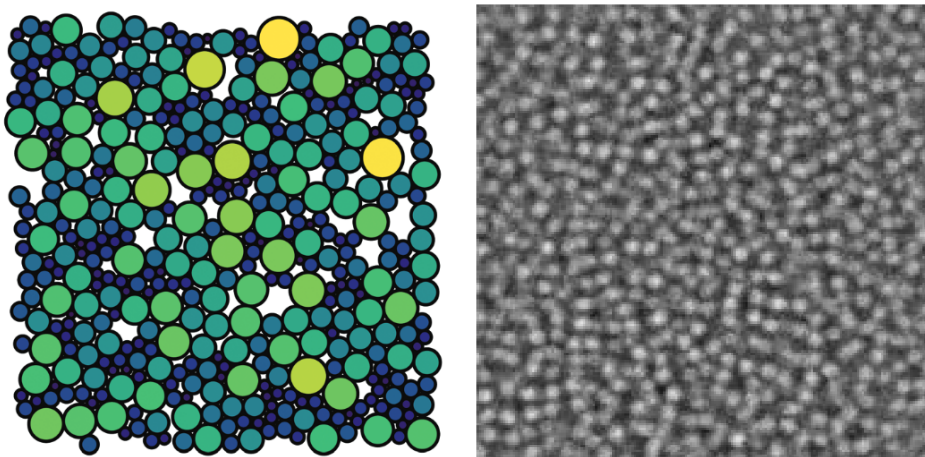


FIGURE 1.1: [2] (left) Simulated packing of particles with the color scheme denoting the number of contacts per particle. [3] (right) A cross-section of micron-sized colloidal particles in suspension.

Nature provides us with a variety of disordered systems, in many fields including chemistry, biology, neuroscience, petroleum science, food science, and computer science, as well as physics from condensed matter to astrophysics and cosmology. Researchers have dedicated significant time and effort to understand disordered systems, with great progress over the years. The result is not only an increase in academic output but also developments and applications in various industries.

Performing experiments, or intervening with the natural world, provides us with an opportunity to achieve degrees of order in a disordered system by applying simple external driving [4, 5]. In this work, we are interested in manipulating disordered particle suspensions in simple ways that can lead to self-organized long-range order in the spatial organization of the particles. Before describing the relevant background on particle suspensions, we review some basic known features of granular materials more generally.

1.1 Granular systems

A granular material is made up of numerous macroscopic particles that typically have only short-range interactions due to particle-particle contacts [6]. As a matter of definition, the particles are considered to be large enough ($> 1\mu m$) so that thermal fluctuation is minimal. Many systems in the real world fall in this category such as a container of marbles or coffee beans, piles of rice, sand dunes, or snow [7–9]. Researchers have carried out extensive research about the mechanical properties of granular systems which can be fluid-like, solid-like, or gas-like, depending on the situation at hand [10, 11]. Such research is important in many applications, for example when designing storage silos for grains, where one wants to be able to calculate the static pressure of the grains inside the wall of the silo to determine the

design and strength of the steel to ensure safety in this form of storage [12]. Physicists, mathematicians, and computer scientists have been focusing on improving simulation techniques to better understand granular systems for decades. This is, in many cases, still challenging; just a gram of fine sand can contain millions of particles irregular in shape. Yet, the outcomes of such research can be transferable and beneficial to many disciplines.

The density of a granular system is an important indicator of its expected behavior. At high density, particles can jam into a state where they no longer flow easily [13, 14]. A jammed system may be mechanically stable and resistant to external stresses [15]. This can occur when the particles are frictional [16, 17] or even when they are frictionless [18–21]. Both situations have been studied extensively in theory [22] and also experiment [14, 23] and numerical simulations [24–27]. This research on jamming not only helps us understand natural phenomena in our daily life but also enables us to utilize jammed materials to do useful things [28].

On the other hand, when a system is less dense, it could become liquid-like or gas-like in a dynamic, flowing state. This kind of state allows for particles to relocate when they are perturbed and the spatial distribution can be different from a totally random disordered system. Studying routes to self-organized states with well-defined properties has been an emerging trend recently. The study of self-organization can help us understand their dynamical behavior even within different non-equilibrium phases, and the phase transitions between them.

1.1.1 Experiments on cyclically sheared suspensions

One particularly interesting case is the self-organization of particle suspensions — collections of hard particles immersed in a liquid. Using cyclic shear as an external

drive, researchers have done a variety of experiments with loosely-packed suspensions [29–31]. In these experiments, they place spherical polystyrene particles in density-matched fluids in coaxial cylinders which will rotate and shear the system periodically (see Fig. 1.2). The fluid has a low Reynolds number so that the inertia of the fluid and the particles are both negligible. These systems show irreversible behaviors when they are sheared. Remarkably, after applying many cycles of low-amplitude shear, the system can reach a steady state where the particle trajectories are reversible and no collisions occur during shearing.

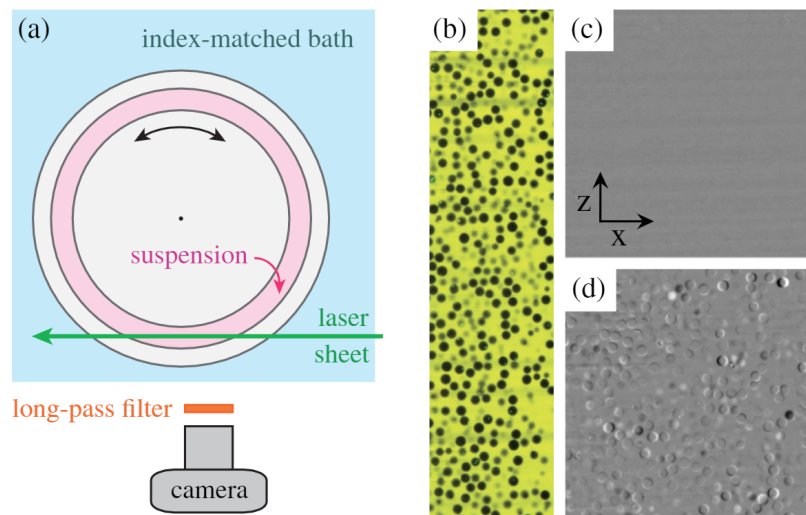


FIGURE 1.2: **Experimental setup used to study self-organization under cyclic shear by Ref. [31].** (a) Setup where two concentric cylinders are used to shear the sample in the gap between them. A laser sheet projected from the side allows a two-dimensional slice to be seen. (b) Image of the suspension. (c) Difference of particle images between two shearing cycles in a reversible state. The image is monotone indicating reversible particle trajectories. (d) Difference of particle images between two shearing cycles in an irreversible state, where light and dark regions are from the net particle displacements.

The steady-state behavior of the system can be controlled by varying the shearing amplitude, γ , given by the maximum rotational displacement of the outer wall divided by the gap size. A system with a volume fraction ϕ can reach a reversible steady state when γ is below a threshold value, γ_c , and it will have only irreversible

steady states when γ is larger. Although early reports invoked long-range hydrodynamic forces or chaos to describe these behaviors [29], it is now generally accepted that the short-range contact interactions between the particles are the important feature of this system, and this physics alone can account for the above macroscopic behaviors [30].

For a suspension system with a packing fraction or driving amplitude lower than the critical one, it will undergo time evolution and enter an “absorbing state”, defined as a configuration where further driving does not change the state. In this state, the initially active system will become inactive after a period of reconfiguration. Beyond the critical threshold, the system is constantly active and the particle trajectories are effectively diffusive at long times. There is a second-order transition of a non-equilibrium system that separate these absorbing states from the diffusive ones [32].

1.1.2 Universality Class of Random Organization

The systems with absorbing states have been studied extensively over a few decades and the closest resemblance to random organization systems are directed percolation (DP) and conserved directed percolation (CDP) in terms of universal scaling behavior. Similarly, DP and CDP systems utilize stochastic processes that evolve in time, to reach absorbing states. As described in [32] and [33], from a reaction-diffusion perspective, DP consists of the following evolving processes which happen in the lattice of sites. One active site can activate nearby sites with some fixed probability. If considering the entire lattice, activation happens continuously, clusters of active sites will propagate indefinitely and the system will be in a steady state. Otherwise, if at any step, no activation can be recorded, the system will stop spread and fall in an absorbing state. Given a dimension $d \geq 2$, one can expect a

critical probability $0 < p_c < 1$ exists which separates these two states. This phenomenon is more general and looks similar to a random organization system. The difference is that in DP, the system evolves through the spread of active sites while a random organization system evolves through the movement of particles. One may notice that the number of active sites in DP is conserved. This brought CDP into people's attention since the number of active sites in CDP is conserved and thus, could be more related to random organization systems. By studying and comparing the universal scaling exponent of these three systems [34, 35], we may be able to solidify possible connections between the random organization system and other stochastic systems.

1.1.3 Previous simulations

To better understand the properties of granular systems and absorbing states, people have developed simulation models to reproduce the same behavior observed in their experiment counterparts.

Based on experimental sandpile models that are trying to explore self-organized criticality (soc), S S Manna has proposed a simpler two-phase simulation model that is set on a square lattice [36]. Each site on this 2D lattice can be occupied by one or more particles or simply stay empty. Whenever a site is occupied by more than one particle, the site is considered to be active and will undergo a random process so that it can become empty or stationary again. The active site will purge each of its particles into its neighboring sites by random selections of directions and these changes may invoke new active sites to its neighbors and then, the random purging of those sites will happen or be calculated during the next simulation cycle. This random process will be conducted from the beginning to the point where all sites are considered stationary in which each site contains at most one particle.

People also found that for the system which undergoes random walks, noise can affect the asymptotic behavior of the random processes in a way that is not local especially with lower dimensionalities involved in the model [37]. The result shows that for a two-dimensional system, the introduction of noise will not only affect its micro behaviors, but also the macro scale evolution of the system. For a granular system, the diffusion process will normally show a power-law decay behavior that is well measured and proved before in different dimensions. With the introduction of the fluctuation, the scaling factor of such power-law decay is changed in a non-trivial way such that it deviates from the result via mean-field theory. In fact, the behavior of the system is change as well as many properties which will be discussed in later chapters.

Inspired by the observed phase transition and the dynamics of particles in experiments, Corte proposed a simpler model of a driven non-equilibrium system that can incorporate the behavior of sheared suspensions and irreversible particle movements. The model is sufficient to provide enough ingredients for us to measure the threshold of phase transition and other behaviors. Corte first introduced a simpler 1D system that consists of a line of particles that will be sheared along the line. Each particle will be sheared with a displacement l and if it collides with another particle, both particles will be given random kicks into random directions along the line and they will redistribute. The whole process is about to apply this rule to all particles one by one and cycle by cycle until no collision is recorded which is called absorbing state or the system enters an actively diffusive state where a relatively constant portion of particles remains active. Use this model, Corte found that for $l > l_c$, there is no absorbing state and it's impossible to let all particles become inactive. But with $l < l_c$, there will be an infinite amount of state that can possibly accommodate all particles without any future collisions happening. The observed

$l_c = 0.91 \pm 0.01L/N$ shows the critical point of this 1D random self-organization system where L is the length of the system and N is the number of particles involved in the simulation. With this critical boundary, the portion of active particles is also measured in active steady states with relation $f_a^\infty \sim [(l - l_c)/l_c]^\beta$ confirming the behavior of the system that is near its critical phase transition point. Then, Corte introduced and described a 2D system that consists of particles with hard walls. The system has no thermal fluctuations and the Reynolds number is low which gives the particles' movement a high damping speed. The entire system is periodic on boundaries and prepared in a random fashion such that the initial positions of particles are totally random but without overlapping. The system is sheared as well to a side so all particles inside will shift by an amount that depends on their vertical locations. Everything is in real space and the particles all have the same diameter when collisions are checked. We can tell two particles collide with each other by calculating the distance of their centers and compare it to their diameter. If they collide, we will give each of them a random kick such that they can fly in different directions by a random amount. This process is continued until no collision can be found within one shearing cycle and the evolution of the system is stopped or can be called that it enters its reversible state. Critical phase transition is observed for such a random organized system when a critical amplitude of shearing is used in the simulation even with different simulation parameters like system size, box shape, boundary conditions, and three-dimensional systems.

Illustration of the proposed 2D simulation model (Fig. 1.3). Within each cycle, particles are sheared to the same direction with different amplitude base on their vertical coordinate and if two particles overlap during the process, they will be given random kicks into random directions. The probability of collision increases with the strain amplitude γ and volume fraction ϕ . When local areas are crowded,

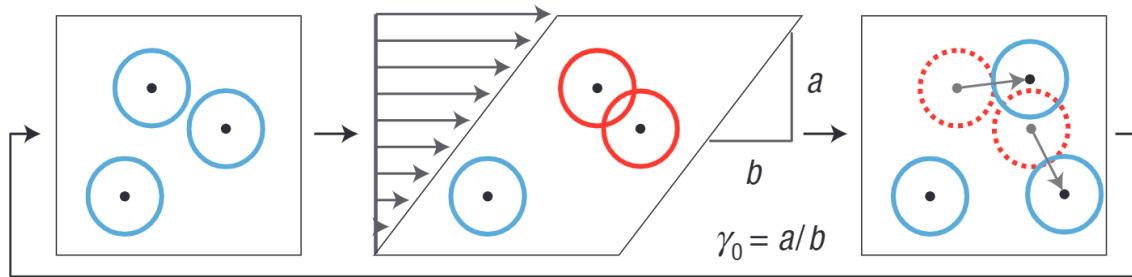


FIGURE 1.3: **Simulation model by [30].** This schematic illustrates the shearing process in a 2D simulation model proposed by Corté to mimic the corresponding experimental setup. After calculating the particle displacements under an affine transformation, one then checks for collisions and marks those particles to be given random kicks before the next cycle.

multiple random kicks are possible if the particle has more than one point of contact with others.

1.2 Hyperuniformity

Disordered systems normally involve randomness which distinguishes them from crystal-like systems. Recently, people have discovered a new state of matter called hyperuniformity in which the systems show order over large distances while still being disordered over small distances. The variations in spatial distribution are suppressed with a higher-order decay factor that lies in between those found in purely random systems and crystals. People suggested that there is hidden order inside hyperuniform systems other than randomness.

To quantify hyperuniformity, we can simply measure the system's structural factors (see Eq.1.1 for definition). For a random granular system, the structural factor should be around 1 for the entire reciprocal space while in a hyperuniform system, the structural factor will approach 0 with a small k .

$$S(\mathbf{k}) = \frac{1}{N} \left| \sum_j e^{i\mathbf{k}\cdot\mathbf{r}_j} \right|^2 \quad (1.1)$$

1.2.1 Hyperuniformity in nature

Researchers also found the hyperuniform pattern in chicken eyes. Specifically, the spatial distribution of its visual cones has a higher order of uniformity than normal disordered systems that are usually seen in biological systems. Different kinds of visual cones will receive different colors of incident light include violet, blue, green, and red (see Fig. 1.4a). Although different types of cones are of a different size, they are actually multi-hyperuniform with respect to the visual cones of the same color (see Fig. 1.4b). This unique pattern ensures the reception of not only the intensity of light but also the color of light to be evenly distributed across the entire visual area of the chicken.

1.2.2 Hyperuniformity in suspensions

To study hyperuniformity and non-equilibrium phase transitions, sheared suspension systems have been proven to be a good candidate that will yield consistent results in both experiment and simulation [39]. With the configuration of the system presented, people can measure its uniformity by evaluating the scaling factor of the variations of spatial distribution or by examining whether the large-scale structural factor will approach zero. Both are robust methods and largely used in research but with the limitation of system size. The variance of fraction is also being measured which is a more suitable method of evaluating uniformity in suspension systems with particles that have different sizes.

To measure the variance of density fluctuations, we need to select a spherical window with radius R and measure the number density of particles inside. Given

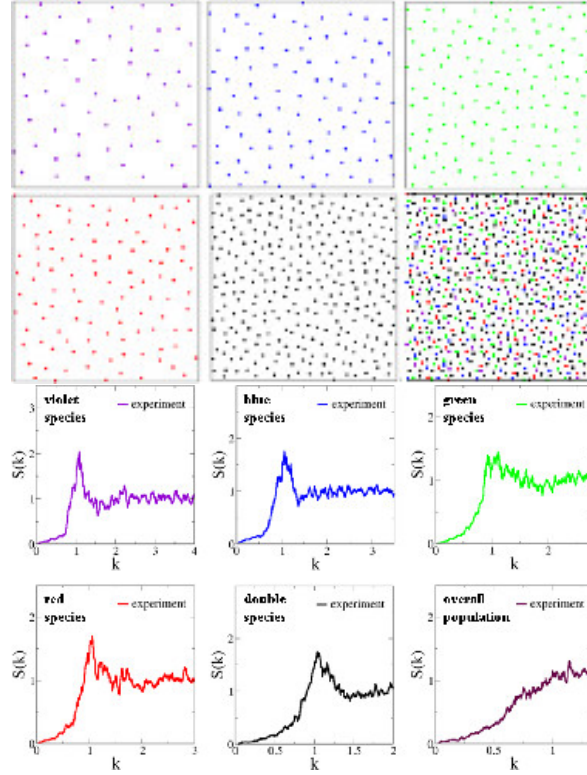


FIGURE 1.4: [38] **Top** Patterns of avian photoreceptors in a chicken's eye. **Bottom** Structural factors of corresponding color cells.

the window volume being R^d where d is the dimension, we have the following relation:

$$\sigma^2(R) \equiv \langle \rho^2(R) \rangle - \langle \rho(R) \rangle^2 \propto R^{-\lambda} \quad (1.2)$$

λ here depends on the type of state of the system. For example, a typical disordered system would have a $\lambda = 0$ while a perfect crystal could have $\lambda = 1$. A hyperuniform system will have a $\lambda \in (0, 1)$ which differs from both of the systems previously mentioned.

1.2.3 Hyperuniformity in other systems

Novel forms of hyperuniform systems are proposed more and more recently including jamming systems [41], two phase system [40] (see Fig. 1.5) and glass [42] in which they all shows the behavior of suppressing large scale fluctuation despite their different realizations. Also, there are applications of hyperuniformity in other field such as computer science and information theory [43].

1.3 Inhomogeneous systems

1.3.1 Driving disordered systems out of inhomogeneous states

Our studies in Chapter 2 and 3 of this thesis are aimed at understanding how disordered materials can evolve to controlled states with well-defined properties when driven in simple ways. Thus, although many studies assume a homogeneous initial state, we explicitly introduce a slow external drive – sedimentation under gravity – to push the system towards an inhomogeneous state. We pair with this an external cyclic drive, applied by the experimenter or simulator, and we seek to understand if and when such driving can return our system to a more uniform state, and if so, how this evolution occurs.

Such research on inhomogeneous conditions is important not just because it is a common condition, but also because it is a way to view the system differently which could provide us more information about the material. For example, in recent research of jamming transitions, researchers have discovered dynamic jamming fronts propagating in a compressed unjammed system [1]. In their experiment, a system containing bidisperse disks is packed uniformly in a rectangle container with the packing fraction below jamming. Then the system is compressed

with a rack from one side with constant velocity. A propagating smooth transition area (front) separates the growing jammed region and diminishing unjammed region.

For a suspension system, we are also interested in inhomogeneous systems for the following reason. In experiments of sheared suspension systems, people usually do density matching so that the particles and stay afloat in fluids. This is essential to make sure that the positions of particles stay unchanged in between shearing cycles and let the dynamics be solely controlled by periodic shears [30]. This condition takes effort to achieve and the shearing time diverges to infinity when the system approaches a critical state.

More realistically, slow sedimentation or creaming will always be present, due to the sinking of heavy grains or floating of light grains. This holds as well in geophysical settings. In Ref. [39], a sedimenting suspension system was proposed and studied to see how cyclic shear and sedimentation compete to produce a steady state. In their paper, they conducted experiments with coaxial cylinders as described before, while letting the particle density be slightly greater than the density of the fluid. This system undergoes a process of shearing and sedimenting until it reaches a steady state in which the density distribution and the top boundary of the particles are fluctuating but at a constant average height. The vertical density distributions were measured and found uniform under slow sedimentation. The authors proposed a quantity to quantify the effective sedimentation velocity as:

$$A = \tau_D / \tau_s = (\pi / \phi_c)^{3/2} d^3 \kappa^2 v_s / 32D \quad (1.3)$$

Given a value of A below a threshold of unity, $A < 1$, the system will show a uniform vertical density distribution in steady state and the top of the particles will maintain at a constant height. This inspired us to further investigate this system

and it might be a good candidate to acquire hyperuniformity in an automated way. Along the way, our systematic and careful simulations revealed a different dimensionless number that is related to the one above but serves as a correction due to different length scales being involved in the problem than what was previously thought.

1.3.2 Density fronts in driven particle systems

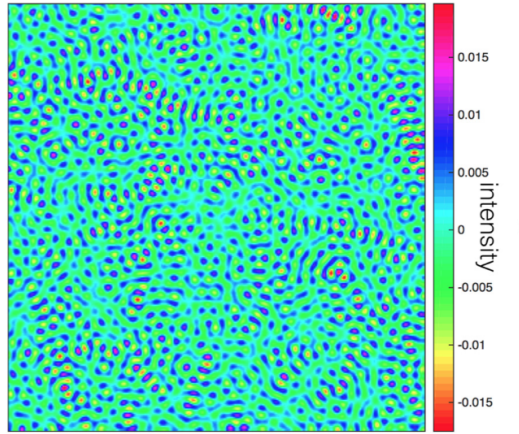
When conducting our numerical simulations of sheared sedimenting suspensions, we noticed some interesting behaviors during the transient: a dense region would build up from the bottom wall and propagate upwards through the system. This behavior looked reminiscent of a feature of dynamic jamming fronts, which have been investigated in experiments in recent years. Here we introduce that system to provide this broader context.

In a recent study of dynamic jamming, Ref. [1] studied the emergent behaviors of a two-dimensional model experiment where hard bi-disperse disks sitting on a 2D plane are compressed by a straight bar from one side (see Fig. 1.8). Initially, the particles are below jamming and randomly distributed. When compressed, the system was found to exhibit a dynamical jamming front that propagates in the direction of the external compression. The jammed area grows with time, as a jamming front propagating towards the uncompressed side. On the dilute side of the front, the particles are in their initial positions; on the compacted side, the system is jammed with a packing fraction that was found to be consistent with the critical jamming density. This propagating front will last until reached the end and the entire system becomes jammed.

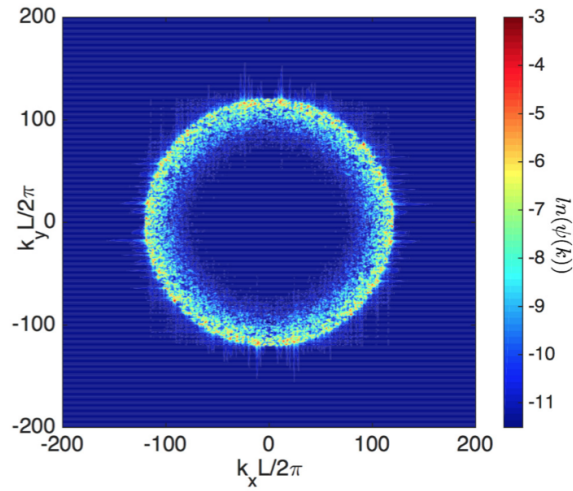
In Chapter 3, we will describe our detailed study of fronts in sheared sedimenting suspensions, and we will draw connections to the jamming of athermal discs.

Interestingly, both non-equilibrium systems share basic features with *equilibrium* interfaces near criticality. Just like a liquid-vapor interface driven to an ordinary critical point, we find that the interface becomes increasingly diffuse near the critical point, mirroring this behavior that was first demonstrated for dynamically jammed grains. Our findings thus show that this phenomenon is perhaps more general than initially conceived.

Researchers have already studied systems with sedimentation in various settings [45, 46]. These systems include sedimentation of passive or active colloidal particles without the presence of shearing. For example, researchers from [46] studied colloidal suspensions in various experimental setups. They found the sedimentation length (of density transition region) is proportional to the effective diffusion of their active particles. The effective temperature of the active colloids could be much higher than the bare temperature with the help of chemical interactions. Also, [45] shows that, with the presence of bacteria, polystyrene particles will sediment at a lower velocity due to the influence of bacterial activity and this effect will be more obvious with higher bacterial concentration. The behavior of sedimentation front changes as well including a suppressed fluctuation which may be due to the increased particle diffusivity. All of these provide us valuable insights into the behavior of the systems, as well as the formation of the sedimentation front. Even though diffusivity could have a direct relation with sedimentation front length, in our sheared particle system, it shows a different picture where the profile of the sedimentation front is not controlled by how active the particles are, but the geometric relations between particles in a large region. This finding could give us a closer look at the intrinsic properties of sheared suspensions and how differently it behaves compared to other colloidal systems.



(a)



(b)

FIGURE 1.5: [40] **Top** An example of stealthy scalar field **Bottom** The measured structural factor over different wavelength plotted in log-scale. A hollow central area indicates reduced fluctuations over the long range.

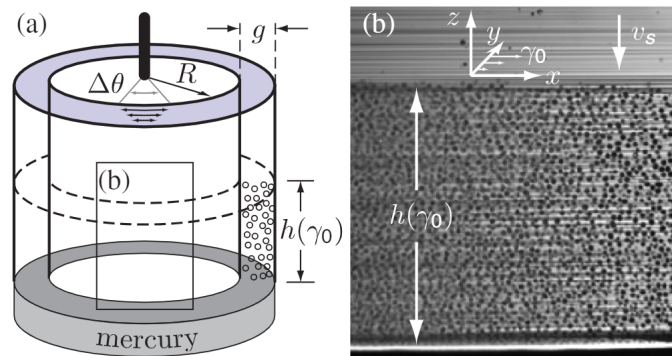


FIGURE 1.6: **Sheared sedimenting suspensions in experiments by Corté *et al.*** (a) Experimental setup from Ref. [39] for the sheared suspension system with sedimentation. (b) Image of the suspension showing a two-dimensional slice illuminated with a laser sheet.

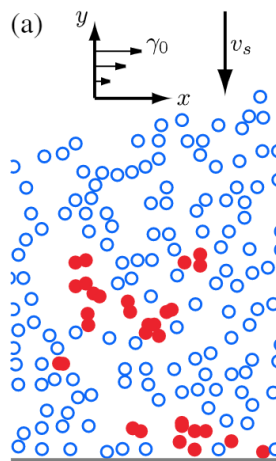


FIGURE 1.7: Illustration of the corresponding simulations from Ref. [39]. Solid particles are packed loosely in a 2D system while being sheared and sedimenting. Red particles are those who encountered other particles during shearing which will be given random kicks.

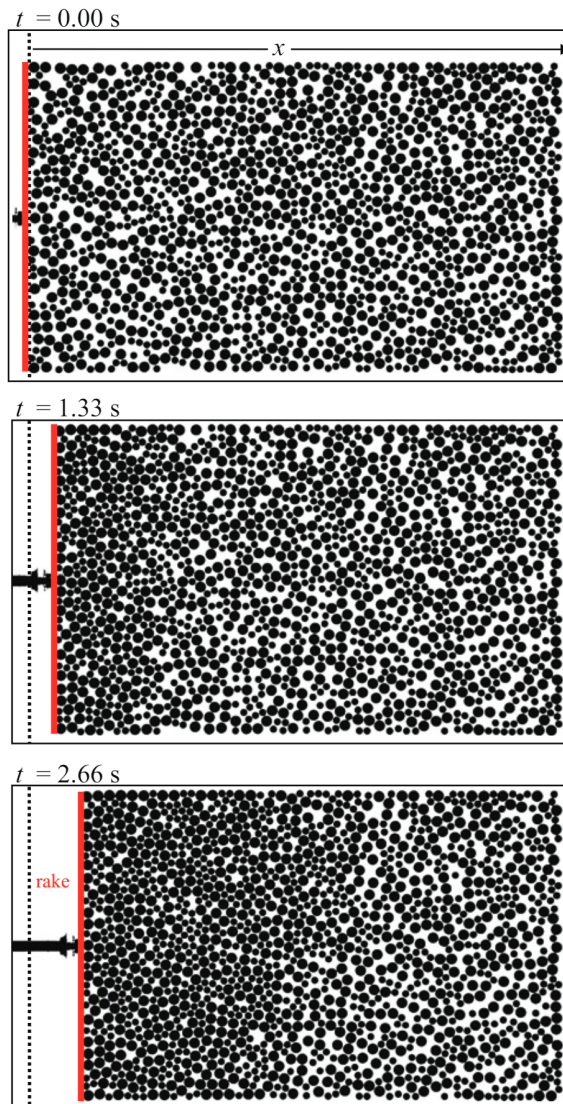


FIGURE 1.8: **Dynamical jamming front in a two-dimensional model experiment, reproduced from Ref. [44].** The image sequence, from top to bottom, shows the evolution of an unjammed system being pushed from one side. A propagating density front can be seen that separates the area of initial packing and the area of jammed packing.

Chapter 2

Hyperuniformity with no fine tuning in sheared sedimenting suspensions

*This chapter is based on a paper published in *Nature Communications*, 9:2836 (2018) with J. M. Schwarz and J. D. Paulsen as co-authors. My contribution was to write original simulation code, perform and analyze the simulations, make analytical calculations, and contribute to the discussion of the results and the writing of the manuscript.*

2.1 Introduction

Particle suspensions can respond to flow in dramatic ways. Steady shear can cause their viscosity to jump by orders of magnitude in some situations, or to plummet in others [47–49]. Interparticle or external forces such as gravity can alter suspension properties over time [50]. These effects put large demands on handling and processing. Thus, methods are desired for obtaining homogeneous particle distributions with predictable mechanical properties, as a platform for further handling. On small lengthscales, one wants to break up aggregates or pockets of high density, since particles moving in close proximity cause significant dissipation. On large

lengthscales, one wants different parts of the sample to have similar particle densities so that the rheological response is stable and reliable.

Recent experiments have shown that non-Brownian suspensions can be driven to well-behaved states simply by applying cyclic, low-Reynolds number shear from the boundaries [29–31, 51, 52]. For small strain amplitudes γ , the particles automatically self-organize into reversible steady states, but for amplitudes larger than a critical value, γ_c , the particles follow irreversible paths indefinitely. An underlying non-equilibrium phase transition has been rationalized by simulations with simple particle kinematics [30] (see the phase diagram in Fig. 2.1a), and has also been shown to directly affect the rheological response in experiments [30, 31, 53]. Further simulations suggest that in such suspensions, the particles should exhibit extremely uniform spatial distributions at the critical strain [54, 55]. These distributions are called “hyperuniform” and are characterized by density fluctuations that decay rapidly as one looks over larger and larger length scales [40, 56, 57]. Shearing at the critical amplitude, γ_c , is thus an attractive method for homogenizing a suspension. Yet, from a practical standpoint it is hindered by requiring precise tuning of the strain amplitude [54].

Here we present a robust method for obtaining a hyperuniform state in a viscous suspension. Based on recent work by Corte *et al.*, [39], we introduce a small density mismatch between the suspending fluid and the particles so that they sediment slowly under gravity. In this situation, cyclic shear was found to re-suspend the particles up to a height where they achieve the critical density, ϕ_c [39]. Our simulations and theoretical arguments show that there is a well-defined regime at low sedimentation speed where this combination of sedimentation and shear serves to homogenize the system. In this regime, density fluctuations are significantly suppressed up to a finite length scale. We show that this length scale is set by small

vertical gradients in the particle concentration, and it can be made arbitrarily large simply by slowing the sedimentation rate. We thereby construct a phase diagram for this “self-organized hyperuniformity”, which is in good agreement with our simulation results.

2.2 Model

We use a simulation model originally developed by [30] This method captures a wide range of behaviors seen in experiments on sheared non-Brownian suspensions, including self-organization [30] and novel memory effects [31, 58]. We place N particles of diameter d in a square box of width L . The box is periodic on the left and right sides, and the top and bottom are hard walls. We use units where $d = 1$ so that lengths are in particle diameters, and we measure time in units of cycles.

Following [39], each cycle consists of particle sedimentation and shear. First, all particles sediment vertically a distance v_s . Shear is then applied in several steps as illustrated in Fig. 2.1b: (i) particles are displaced with an affine transformation, $(\Delta x, \Delta y) = (\gamma y, 0)$, where y is the distance of the particle to the bottom wall, (ii) particles are returned to their original (unsheared) positions, and (iii) particles that overlap during this transformation are given a kick in a random direction with a magnitude chosen uniformly between 0 and ϵ , where $\epsilon = 0.5$ except where otherwise stated. The effect of the shearing is to make particles collide that are within an interaction region, like the one sketched in Fig. 2.1c. (In previous studies, varying the kick size or collision kinematics did not change the qualitative results [59].)

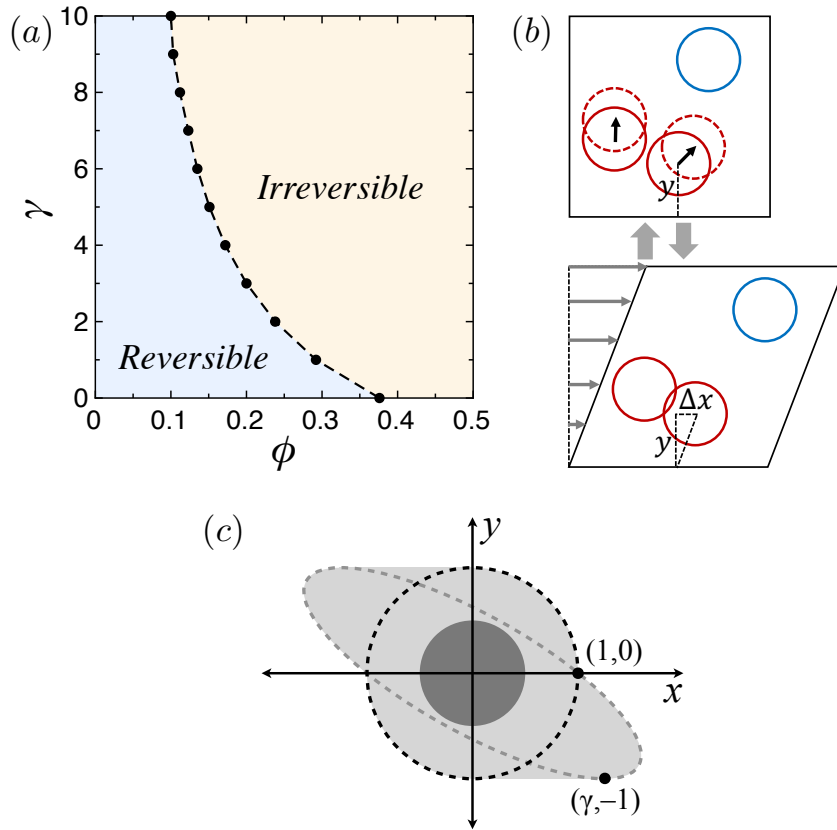


FIGURE 2.1: **Sheared non-Brownian suspension model after Ref. [30].** **(a)** Phase diagram showing reversible steady states at low volume fraction, ϕ and strain amplitude, γ . Outside this region, a finite fraction of particles collides during each cycle in the steady state. Dashed line: Critical phase boundary. Data show the largest γ where we obtain a reversible state in simulations with $N = 10186$ particles. **(b)** Simulation algorithm. In each shear cycle, particles are displaced a horizontal distance $\Delta x = \gamma y$ and then returned to their initial positions. Particles that overlap (red) are given random kicks, to simulate local irreversibility due to collisions. **(c)** Interaction region around a particle. A second particle with its center anywhere inside the dashed circle will overlap with the particle at the origin (shown as a dark circle); they would both receive a random kick. Shearing the system expands the interaction region to the entire shaded area (shown for one value of γ), which contains the points that are covered by continuously shearing the dashed circle up to strain amplitude γ and back.

2.2.1 Implementation

Here, we provide pseudo-code for actual simulation programs. The code represents one instance of simulation and multiple (5 ~ 50) have been done for averaging with each setting.

Algorithm 1 Initialization

```
1: while  $\phi < \phi_0$  do
2:   while  $n$  do valid
3:      $x \leftarrow \text{random}(0, W)$ 
4:      $y \leftarrow \text{random}(0, H)$ 
5:     if not periodical boundary then
6:       if distance from  $(x, y)$  to any boundary  $< \text{radius}$  then
7:         continue
8:       if distance from  $(x, y)$  to nearby particles  $\geq \text{diameter}$  then
9:         valid  $\leftarrow$  True
10:    update  $\phi$ 
```

Algorithm 2 Collision Check

```
1: for particle  $i$  from 1 to  $N$  do
2:   for nearby particles  $j$  from 1 to  $n$  do
3:      $(x, y) \leftarrow$  particle  $i$  coordinates
4:      $(x', y') \leftarrow$  particle  $j$  coordinates
5:      $(\Delta x, \Delta y) \leftarrow (x' - x, y' - y)$ 
6:     if  $|\Delta y| > 2r$  then continue
7:     if  $\Delta y > 0$  &  $\Delta x > -\sqrt{4r^2 - \Delta y^2} - \gamma\Delta y$  then
8:       collision  $i, j \leftarrow$  True
9:     if  $\Delta y < 0$  &  $\Delta x < \sqrt{4r^2 - \Delta y^2} - \gamma\Delta y$  then
10:      collision  $i, j \leftarrow$  True
```

2.3 Self-organized criticality

Corté et al. [39] recently showed that for sufficiently slow sedimentation a critical state is automatically reached, offering a rare example of self-organized criticality

Algorithm 3 Random Kick

```
1: for particle 1 to  $N$  do
2:   if collision during shear then
3:      $\theta \leftarrow \text{random}(0, 2\pi)$ 
4:      $x \leftarrow x + \epsilon \cos(\theta)$ 
5:      $y \leftarrow y + \epsilon \sin(\theta)$ 
6:     if periodical boundary then
7:       if  $x < 0$  then  $x \leftarrow x + W$ 
8:       if  $x > W$  then  $x \leftarrow x - W$ 
9:       if  $y < 0$  then  $y \leftarrow y + H$ 
10:      if  $y > H$  then  $y \leftarrow y - H$ 
11:     else
12:       if  $x < r$  then  $x \leftarrow 2r - x$ 
13:       if  $x > W - r$  then  $x \leftarrow 2W - 2r - x$ 
14:       if  $y < r$  then  $y \leftarrow 2r - y$ 
15:       if  $y > H - r$  then  $y \leftarrow 2H - 2r - y$ 
```

Algorithm 4 Combined with Sedimentation

```
1: Initialization()
2:  $cycle = 0$ 
3: while  $cycle < \text{cutoffcycle}$  do
4:   for particle 1 to  $N$  do
5:      $(x, y) \leftarrow (x, y - v_s)$ 
6:     if  $y < r$  then  $y = r$ 
7:   Collision Check()
8:   Random Kick()
9:    $cycle \leftarrow cycle + 1$ 
```

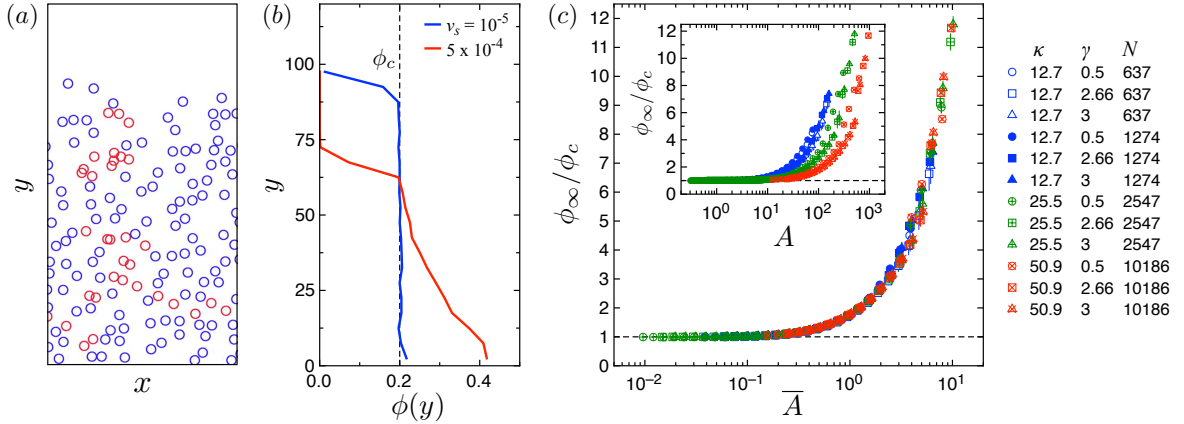


FIGURE 2.2: **Self-organized criticality at low sedimentation speed.** (a) Snapshot of system in steady state. Red particles are colliding in the current cycle. (b) Area fraction (plotted on the x axis) versus vertical coordinate, y , at low and high sedimentation velocity v_s , with $N = 2547$, $\gamma = 3.0$, $\kappa = 25.5$, and $L = 100$. Vertical dashed line shows $\phi_c(\gamma = 3) = 0.20$. (c) Scaled steady-state volume fraction ϕ_∞/ϕ_c , measured over a wide range of system parameters (κ , γ , and N as shown in legend) and velocities ($10^{-5} < v_s < 10^{-2}$). *Inset*: Measurements versus the parameter $A = (\pi/\phi_c)^{3/2} d^3 \kappa^2 v_s / 32D$, proposed by Ref. [39]. The data is not collapsed. *Main*: The data collapse when replotted versus \bar{A} (Eq. 2.1). For $\bar{A} \ll 1$ (low sedimentation speed), the steady-state volume fraction ϕ_∞ is equal to the critical value ϕ_c . Error bars are from fluctuations in system height in the steady state.

seen in both simulation and experiment [60]. This behavior occurs when the steady-state density of the particles is equal to the critical density, ϕ_c , and it can be anticipated from simple arguments. At any v_s , the particles settle to a steady-state height where sedimentation and diffusion balance, as pictured in Fig. 2.2a. For slower sedimentation, this balance leads to a higher height, as shown by the vertical density profiles in Fig. 2.2b. Hence, at lower v_s , the average volume fraction throughout the pack in the steady state, ϕ_∞ , is also lower. Crucially, because the diffusion is driven by collisions, the particles stop spreading apart when they are just far enough away to stop colliding, so the density cannot decrease below ϕ_c . Thus, $\phi_\infty \rightarrow \phi_c$ as $v_s \rightarrow 0$.

Quantitatively, the critical density is achieved when a suitably chosen sedimentation timescale, τ_s , is much smaller than a diffusion timescale, τ_D . Corté et al. [39]

proposed that τ_s is set by the time to sediment a mean particle spacing (a distance $\sqrt{\pi d^2/4\phi}$), and τ_D is the time for a particle to diffuse the system height (i.e., $\tau_D = h^2/4D$ where D is the coefficient of diffusion for a non-sedimenting system at $\phi = 2\phi_c$, and $h = \pi d^2\kappa/4\phi$ is the system height with $\kappa = N/L$ being the linear density of particles along the x axis). In a critical state where $\phi = \phi_c$, the ratio of these timescales is: $A = \tau_D/\tau_s = (\pi/\phi_c)^{3/2}d^3\kappa^2v_s/32D$.

The inset to Fig. 2.2c shows our measurements of ϕ_∞/ϕ_c , where we vary velocity v_s , linear density κ , strain amplitude γ , and system size N over a broad range. The data indeed approach 1 for small A , but they are clearly not collapsed. (Reference [39] set their expression for A to be 8 times this value; this merely shifts all the data along the x axis by a fixed amount.)

We propose that the timescales for diffusion and sedimentation should instead be considered over the same length scale. Taking τ_D and τ_s as the timescales for particle transport over the system height, we obtain:

$$\bar{A} = \frac{\tau_D}{\tau_s} = \frac{\pi}{16} \frac{d^2\kappa v_s}{\phi_c D}, \quad (2.1)$$

which serves as a non-dimensional sedimentation speed. This expression produces an excellent collapse of the data, as shown in Fig. 2.2c.

2.3.1 Dependence of self-organized criticality on collision rule.

The simulation model for cyclically-sheared viscous suspensions that we use in this work was originally developed by [30] to study self-organized reversible states. Variants of this model have been studied in recent years. Reference [59] studied a wide range of driving and collision rules to test for the robustness of results on memory formation; [55, 61] used isotropic swelling in place of shear as a simpler

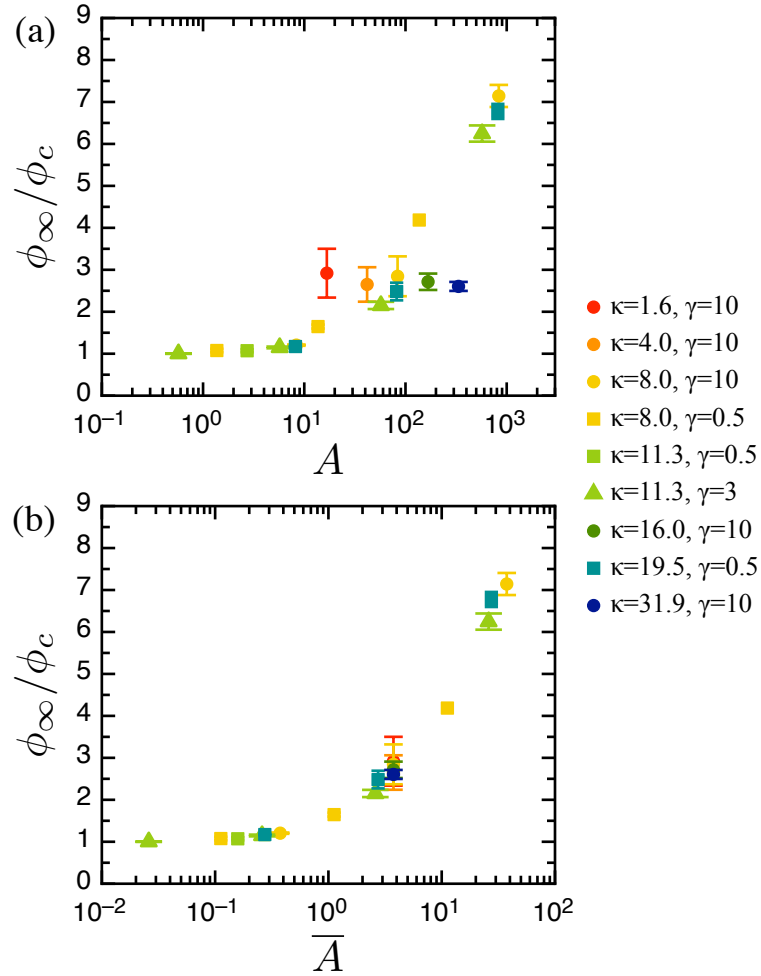


FIGURE 2.3: **Results for multiple kicks.** Scaled steady-state density in a suspension sedimenting at velocity $10^{-4} < v < 10^{-1}$, sheared at strain amplitude γ . We use $N = 1000$, $\epsilon = 0.5$, and $1.6 < \kappa < 31.9$. The diffusion constant D is set to 0.0414, the value obtained by Corté *et al.* [39]. **(a)** The data only approximately collapse with $A = (\pi/\phi_c)^{3/2}d^3\kappa^2v_s/32D$, the scaling proposed by [39]. **(b)** The data collapse when plotted versus $\bar{A} = \pi d^2\kappa v_s/16\phi_c D$.

method for studying the critical transition, and [37, 59] used center-of-mass conserving collisions to suppress long-range diffusion.

Here we probe one aspect of these kinematics in order to make a more precise comparison to previous results [39]. In a dense portion of the sample, a particle can encounter multiple other particles during a single cycle. In the present work, we give just one kick to such a particle, whereas Corté *et al.* [39] gave one kick for each particle encountered, which increases diffusion rates in dense regions.

We find that the scaling for obtaining the critical density under sedimentation does not change between these two models. Figure 2.3 shows ϕ_∞/ϕ_c for simulations we performed with the “multiple kick” rule. The data only approximately collapse when plotted versus A , but they collapse cleanly when plotted versus \bar{A} . To contrast the two expressions, in 5 of these simulations we kept the product κv_s constant while varying κ from 1.6 to 31.9 (with $\gamma = 10$), so that $\bar{A} \propto \kappa v_s$ is fixed but $A \propto \kappa^2 v_s$ varies. Those points show that the data are better collapsed by \bar{A} , as we found for single kicks. This test also serves as a further systematic check on our results, as the two simulation codes were written independently by two of us (J.W. and J.D.P.).

2.3.2 Structure factor

At low sedimentation speed, the suspension is in a critical state, characterized by a power-law distribution of avalanches that are set off by individual collisions [39]. Although a suggestive connection has been identified between criticality and hyperuniformity [54], there is presently no deductive link. To see whether hyperuniformity can survive the dynamics of sedimentation and resuspension, we now look for hyperuniformity in our simulations. Following previous studies [52, 54, 55, 62,

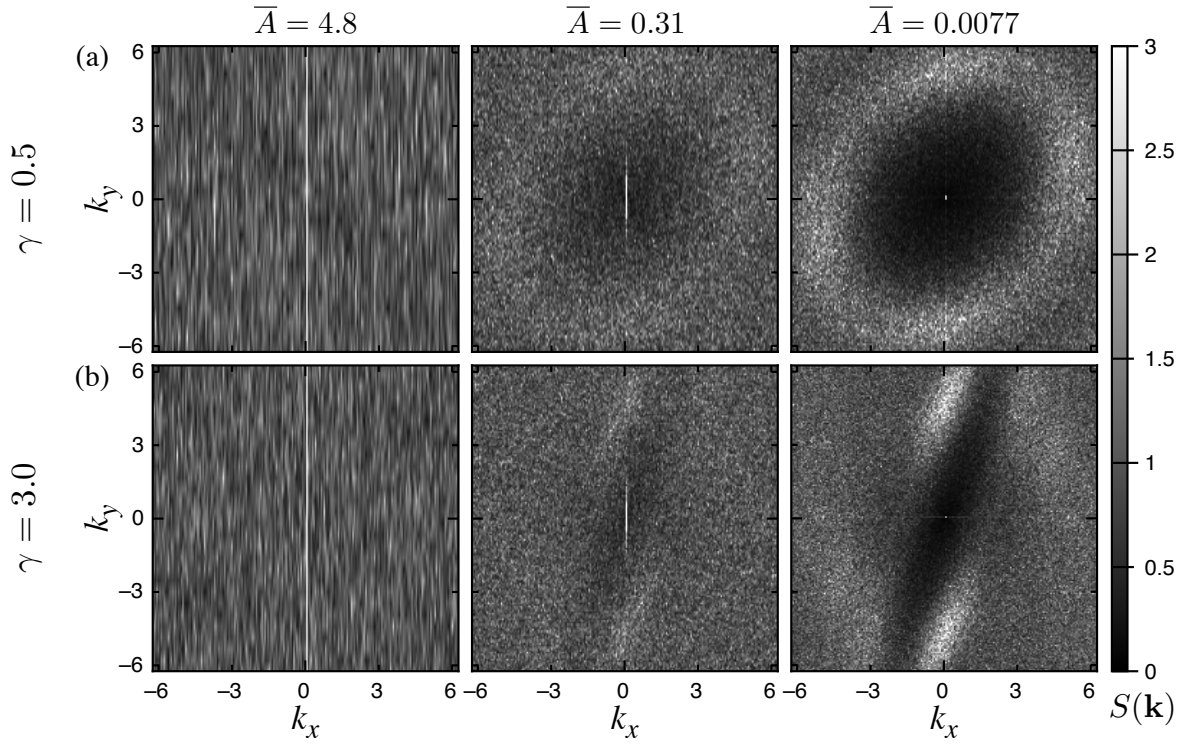


FIGURE 2.4: **Static structure factor.** $S(\mathbf{k})$ measured in 2D simulations with $N = 4827$, $\kappa = 34.1$, and $\varepsilon = 0.5$, at three values of \bar{A} and in the steady state. Values are calculated using Eq. 2.2 at wavevectors k_x and k_y where an integer number of wavelengths fill the region populated by the particles. The sum is performed over the bottom 99% of the particles to avoid the diffuse boundary layer at the top of the sample. **(a)** Results for $\gamma = 0.5$. At low \bar{A} , a region with low intensity develops near the origin, signaling hyperuniformity. (This region is not circular because of the anisotropic driving.) **(b)** Results for $\gamma = 3$. Despite larger anisotropy in the structure, hyperuniformity occurs at low \bar{A} .

63], we consider the structure factor defined by:

$$S(\mathbf{k}) = \frac{1}{N} \left| \sum_j e^{i\mathbf{k}\cdot\mathbf{r}_j} \right|^2, \quad (2.2)$$

where \mathbf{k} is a two-dimensional (2D) wavevector and \mathbf{r}_j is the location of the center of the j^{th} particle. Density fluctuations over large distances in real space affect $S(\mathbf{k})$ near the origin in reciprocal space; the hallmark of hyperuniformity is that $S(\mathbf{k}) \rightarrow 0$ as $\mathbf{k} \rightarrow 0$.

Figure 2.4 shows our measurements of the structure factor for two values of the strain amplitude, γ , and three values of the non-dimensional sedimentation speed, \bar{A} . Each panel is an average of 5 systems analyzed at a single snapshot in time after the system has reached a steady state. For large sedimentation speeds, $\bar{A} > 1$, the data are featureless and show that density fluctuations exist on all length scales. (The thin white band is due to vertical density gradients.) At smaller \bar{A} , the intensity begins to decrease near the origin. Hyperuniformity is clearly present at $\bar{A} = 0.0077$. Crucially, both strain amplitudes produce a hyperuniform state with no fine tuning of the driving.

2.3.3 Density fluctuations in real space

To probe the system further, we investigate density fluctuations in real space. We measure the particle number density in circular regions of diameter ℓ , centered at random locations. As before, we avoid the diffuse boundary layer at the top of the sample by staying in the bottom 99% of the particles. Denoting the variance of the number density over these samples by $\sigma_\rho^2(\ell) \equiv \langle \rho^2(\ell) \rangle - \langle \rho(\ell) \rangle^2$, hyperuniformity

is characterized by the rate of decay of σ_ρ^2 with respect to window size:

$$\sigma_\rho^2(\ell) \propto \ell^{-\lambda}, \quad (2.3)$$

with λ greater than the system dimensionality.

Figure 2.5a shows $\sigma_\rho^2(\ell)$ for several sedimentation speeds, v_s . At the lowest v_s , we observe hyperuniformity with a scaling exponent of $\lambda = 2.60 \pm 0.04$. (The data are also consistent with $\sigma_\rho^2(\ell) \sim \ell^{-3} \log(\ell)$, a scaling that occurs in jammed packings [64, 65] and in an isotropic version of the sheared-suspension model in the presence of noise [37].) Notably, our measurements at low velocity show the same variance scaling as our simulations of non-sedimenting particles at $\phi = \phi_c$ (bottom curve of Fig. 2.5c with $\lambda = 2.60$). At larger velocities, number-density fluctuations gradually increase, first at long lengthscales and then moving down to smaller ℓ .

The tails at large ℓ are due to the finite size of the system. In particular, when the window size ℓ is comparable to the height of the suspension bed, the sampling windows are forced to overlap. This reduces the variation in number density as the measurements are not independent. This effect was identified in [62]; we investigate it further in the next section. The steady-state height of the bed is also shorter at larger velocities, which limits the data to a smaller range of ℓ .

To demonstrate a hyperuniform scaling of the variance up to even larger lengthscales, we model an analogous system in one dimension (1D). The system is oriented vertically and sedimentation is applied as in the 2D case (see Supplementary Video 3). Following previous work on such 1D models [30, 66], any particle that is within an interaction distance $\gamma = 1$ of another receives a random kick that is up or down with a magnitude between 0 and ϵ . Figure 2.5b shows $\sigma_\rho^2(\ell)$ measured in the steady state for different sedimentation speeds. Hyperuniform scaling is observed over three decades in length with $\lambda = 1.44 \pm 0.02$.

2.3.4 Finite size effects

In Fig. 2.5, the variance of the number density is observed to fall off rapidly at large ℓ . This occurs when the window size, ℓ , is a significant fraction of the narrowest system dimension, causing the sampling windows to overlap. The samples are therefore not statistically independent, so the variation in the number density is suppressed. This effect has been investigated previously for small variations in system size [62].

Here we study this effect by probing a large range of system sizes in simulations without sedimentation. We produce hyperuniform distributions of particles by shearing a square system of side length L near the critical amplitude γ_c . We measure the variance of the number density, which decays as $\ell^{-\lambda}$ with $\lambda \approx 2.60$. We then cut subsystems of side length $L' < L$ out of the original system, and we measure the variance in the same manner. This is repeated for a total of 6 system sizes, with ratios L'/L from 0.022 to 1. Each curve is averaged over 42 systems to suppress noise.

The results are shown in the inset to Fig. 2.6. Each curve follows the same scaling with ℓ and falls off rapidly when ℓ approaches L' . We shift the curves by rescaling the x axis by L/L' and the y axis by $(L/L')^{2.60}$. Remarkably, all the data fall onto a single master curve, suggesting that the effect is universal.

2.4 Loss of hyperuniform scaling by linear density gradients

In both 2D and 1D, the loss of hyperuniformity at high sedimentation speeds is no surprise — these systems show large vertical density gradients at high v_s , as shown already in Fig. 2.2b and seen in earlier work on this model [39]. Nonetheless, one

wants to know how small the velocity must be to prepare a system in a hyperuniform state. In the remainder of this Chapter, we build up a general quantitative framework that answers this question. Our approach is to split the total variance of the number density into two additive terms: one from the statistics of the particles in a critical state, $\sigma_\rho^2(\ell)_c$, and the other capturing the effect of a global concentration gradient. That is,

$$\sigma_\rho^2(\ell)_{\text{total}} = \sigma_\rho^2(\ell)_c + \sigma_\rho^2(\ell)_{\text{grad}}. \quad (2.4)$$

Our main task is to establish a quantitative description of $\sigma_\rho^2(\ell)_{\text{grad}}$. As a result of this analysis, we establish a finite lengthscale ℓ_H beyond which hyperuniform scaling is lost.

To this end, we study the effect of system-spanning density gradients in a well-controlled setting. First, we generate hyperuniform distributions of particles by shearing a non-sedimenting system at $\gamma \approx \gamma_c$ until it reaches a reversible steady state. We then adjust the y positions of these particles to create a uniform vertical density gradient. The mapping is uniquely determined by requiring a density map $\phi_0 \rightarrow \phi(y) = \phi_0 + |\partial\phi/\partial y|(h - 2y)/2$ on a continuum system with constant density ϕ_0 , where $0 < y < h$. To see this, we denote the initial uniform distribution by $\phi_L(y) = \phi_0$ and the target distribution by $\phi_R(y) = ay + b$, as drawn in Fig. 2.7. The total area under these curves must be identical, so $b = \phi_0 - aH/2$, where H is the height of the system. The mapping must also conserve mass; for a region from the bottom of the system up to a height y , we have:

$$\int_0^y \phi_L(y) dy = \int_0^{y'} \phi_R(y) dy, \quad (2.5)$$

where the point at height y maps to height y' . Plugging in the expressions for ϕ_L and ϕ_R and performing the integral, we get:

$$\phi_0 y = \frac{1}{2} a y'^2 + \left(\phi_0 - \frac{aH}{2} \right) y'. \quad (2.6)$$

Solving for y' , we retrieve the mapping:

$$y' = \frac{H}{2} - \frac{\phi_0}{a} + \sqrt{\frac{2\phi_0 y}{a} + \left(\frac{H}{2} - \frac{\phi_0}{a} \right)^2}, \quad (2.7)$$

where $a = \partial\phi/\partial y$ is the target vertical density gradient.

We measure the variance of these distorted systems, shown in Fig. 2.5c for different values of the gradient, $|\partial\phi/\partial y|$. As in the full sedimentation simulations, the variance is affected at large ℓ first, and at gradually shorter lengths as the perturbation increases.

2.4.1 Variance of density in a continuous system with a linear density gradient

We can understand these variance curves from simple arguments. We calculate the variance of a continuous density field with a uniform vertical gradient in a box of height H and width L , with periodic boundary conditions along x . The density at position (x, y) is given by:

$$\phi(x, y) = \phi_0 + \frac{\phi_b - \phi_t}{2} \left(1 - \frac{2y}{H} \right), \quad (2.8)$$

where ϕ_b and ϕ_t are the densities at the bottom and top of the system, and $\phi_0 = (\phi_b + \phi_t)/2$ is the mean density. The variance of the number density is defined by:

$$\sigma_\rho^2(\ell) = (\phi(x, y) - \phi_0)^2 f(x, y) dx dy, \quad (2.9)$$

where the probability density function is given by $f(x, y) = 1/L(H - \ell)$, since the sampling window cannot cross the top or bottom of the simulation region (i.e., $\ell/2 < y < H - \ell/2$). Plugging in and evaluating, we find:

$$\sigma_\phi^2(\ell)_{\text{grad}} = \frac{1}{12} \left(\frac{\partial \phi}{\partial y} \right)^2 (H - \ell)^2, \quad (2.10)$$

where $\partial \phi / \partial y = (\phi_t - \phi_b) / H$. Then, converting from concentration to number density, we find:

$$\sigma_\rho^2(\ell)_{\text{grad}} = \frac{4}{3\pi^2} \left(\frac{\partial \phi}{\partial y} \right)^2 (H - \ell)^2, \quad (2.11)$$

The total variance in the discrete particle system is obtained by adding this result to the variance of the corresponding system with no concentration gradient (i.e., $\partial \phi / \partial y = 0$), as anticipated by Eq. 2.4. Figure 2.5c shows that this prediction is in excellent agreement with the data across all lengthscales and over a large range of gradients.

The similarity between Fig. 2.5a,b for sedimentation simulations and Fig. 2.5c for the effect of a simple linear distortion is striking. This result suggests that the density fluctuations in this system can be largely accounted for by understanding these concentration gradients. We now move to quantify the strength of the vertical concentration gradients that arise in the model.

2.4.2 Vertical density profile

We now derive the vertical density profile, $\phi(y)$, in a simplified model of a sheared sedimenting simulation. We start by solving the simpler case of particles randomly diffusing with diffusion constant D while sedimenting at an average speed v_s . In the steady state, the flux through a horizontal line at any height must be zero. This gives:

$$\phi(y)v_s = -D\phi'(y), \quad (2.12)$$

where the left-hand side describes transport due to sedimentation and the right-hand side describes transport due to diffusion. This equation can be solved to give:

$$\phi(y) = \phi(0)e^{-v_sy/D}. \quad (2.13)$$

We additionally assume that $\phi(y) = 0$ above some finite steady-state height h_∞ .

The coefficient $\phi(0)$ is determined from the boundary conditions. All N particles are contained in a box of width L and height h_∞ , so:

$$\frac{\pi}{4}d^2\kappa = \int_0^{h_\infty} \phi(0)e^{-v_sy/D}. \quad (2.14)$$

Solving for the coefficient, we get:

$$\phi(0) = \frac{\pi d^2 \kappa v_s}{4D(1 - e^{-v_sh_\infty/D})}. \quad (2.15)$$

2.4.3 Magnitude of vertical density gradient

We measure the mean steady-state density gradient, $|\Delta\phi/\Delta y|$, by fitting a straight line to the density profile. We fit the middle 60% of the particles to avoid boundary effects. Figure 2.9 shows our measurements as a function of \bar{A} . The data are only approximately collapsed, suggesting that the vertical density gradient is determined by a different balance than what was computed in Eq. 2.1 for the average density.

In the simple scenario where particles are constantly diffusing in a gravitational field, the vertical density profile is exponential: $\phi(y) \propto e^{-v_s y/D}$ [67]. In the present simulation model, at the height where the density reaches ϕ_c , the particles undergo few collisions so that diffusion essentially turns off (see Fig. 2.2b and [39]). Thus, we approximate the density profile as an exponential up to a finite height where $\phi = \phi_c$, with $\phi = 0$ above that level. This constraint plus the conserved number of particles yields a unique profile $\phi(y)$, with a vertical density gradient given by:

$$\phi'(y) = -\frac{\pi d^2 \kappa v_s^2}{4D^2} \frac{e^{-v_s y/D}}{1 - e^{-v_s h_\infty/D}}. \quad (2.16)$$

In a critical state with $h_\infty = h_c = \pi \kappa d^2 / 4\phi_c$, the second term reduces to $e^{-2\bar{A}} / (1 - e^{-2\bar{A}})$ at half the pack height, $y = h_\infty/2$. This expression is order 1 at $\bar{A} = 1$, but it varies widely as a function of \bar{A} . Nonetheless, the first factor in Eq. 2.16 collapses the data very well, as shown in Fig. 2.9. Fitting for the numerical prefactor, we find:

$$\left| \frac{\Delta\phi}{\Delta y} \right| \approx 0.27 \frac{d^2 \kappa v_s^2}{D^2}. \quad (2.17)$$

2.4.4 Phase diagram

We can now demonstrate how hyperuniformity is achieved for small density gradients in the full simulations. We insert Eq. 2.17 for the vertical density gradient into Eq. ?? for the variance of a hyperuniform system subjected to a linear gradient distortion. We take $\ell \ll h$ (thereby ignoring boundary effects due to the window encountering the edge of the system), and we assume a critical state where $h_\infty = h_c$. Plugging in and expressing in terms of \bar{A} , we get:

$$\sigma_\rho^2(\ell)_{\text{total}} \approx \sigma_\rho^2(\ell)_c + 4.1\bar{A}^4\phi_c^2. \quad (2.18)$$

This simple expression shows that at a fixed lengthscale ℓ , the total variance is the sum of a constant term from the statistics of the critical state, $\sigma_\rho^2(\ell)$, and a term that depends on sedimentation via the product $\bar{A}\sqrt{\phi_c}$.

To test this result, Fig. 2.10a shows the variance σ_ρ^2 measured at a lengthscale $\ell = 10$ in our sedimentation simulations, as a function of $\bar{A}\sqrt{\phi_c}$. The data are collapsed, and they compare well with Eq. 2.18 up to moderate velocities. In Fig. 2.10b, we plot the magnitude of the scaling exponent, λ , measured locally at $\ell = 10$. The data are again collapsed at low and moderate velocity, and they show a hyperuniform scaling (i.e., $\lambda > 2$) for sufficiently small $\bar{A}\sqrt{\phi_c}$.

We construct a phase diagram by measuring the local scaling of σ_ρ^2 in the same manner, as a function of ℓ and $\bar{A}\sqrt{\phi_c}$. In particular, Fig. 2.10c shows our measurements of the lengthscale ℓ_H where λ falls below 2, marking a phase boundary between hyperuniform and non-hyperuniform scaling. This lengthscale becomes longer for smaller v_s (and hence smaller \bar{A}) for the simple reason that hyperuniform scaling is lost when density fluctuations due to the vertical density gradient (scaling as $\bar{A}^4\phi_c^2$ independent of ℓ) become comparable to the density fluctuations

in the critical state ($\sigma_c^2(\ell) \sim \ell^{-2.60}$), as anticipated by Eq. 2.18. Equating these two terms yields the scaling: $\ell_H \sim (\bar{A}\sqrt{\phi_c})^{-4/2.60} \approx (\bar{A}\sqrt{\phi_c})^{-1.54}$.

Improving on this scaling result, we can predict the precise location of this phase boundary by solving for the lengthscale ℓ_H where the local scaling exponent of Eq. 2.18 (i.e., ℓ times the logarithmic derivative of Eq. 2.18) is equal to $\lambda = 2$. This computation yields:

$$\ell_H \approx 0.22(\bar{A}\sqrt{\phi_c})^{-1.54}, \quad (2.19)$$

which agrees very well with our data, as shown in Fig. 2.10c. We also obtain a good description of the 1D simulations by applying the same arguments in that setting (see the following section). Three measured numerical values have entered into this calculation of the phase boundary: the numerical prefactor and exponent of $\sigma_\rho^2(\ell)$ in the critical state, and the numerical prefactor for the size of the vertical density gradients in Eq. 2.17. The prediction is otherwise completely constrained by our physical arguments.

Finally, we note that all the data in Fig. 2.10a-c across a wide range of strain amplitude, $0 < \gamma < 10$, are in reasonable agreement. Although there are some differences for larger velocities in Fig. 2.10c, the data for different γ merge together as the velocity decreases. Hence, for the simulation algorithm and protocol studied here, there seems to be no practical limit on the value of γ for preparing a hyperuniform sample. We have even considered the case where $\gamma = 0$, in which particles receive kicks when they come in contact with each other. Although this limit is not so physical, it suggests that all that is needed is a source of displacements for particles that are sufficiently close.

2.5 One-dimensional model

We can predict the loss of hyperuniform scaling in the 1D system by tailoring our arguments to this dimension. First, the nondimensional \bar{A}_{1D} is given by:

$$\bar{A}_{1D} = \frac{1}{2} \frac{dNv_s}{\phi_c D}. \quad (2.20)$$

Eq. 2.1 (for the effect of a linear gradient on the variance of the number density) applies to 1D with no modifications, as it already averages over the x coordinate. The scaling for vertical density gradients is modified to:

$$\left| \frac{\Delta\phi}{\Delta y} \right| \approx 0.36 \frac{dNv_s^2}{D^2}, \quad (2.21)$$

where we obtain the numerical prefactor by fitting to the data, shown in Fig. 2.11a.

Adding the variance due to the vertical density gradient to the variance in the critical state without sedimentation, we get for the total variance in 1D:

$$\sigma_\rho^2(\ell) \approx \sigma_c^2(\ell) + 0.17 \bar{A}_{1D}^4 \phi_c^2. \quad (2.22)$$

We then solve for the length-scale ℓ_H where ℓ times the logarithmic derivative of Eq. 2.22 (i.e., the local scaling exponent) is equal to $\lambda = 1$, where we use $\sigma_c^2(\ell) \approx 0.15\ell^{-1.44}$ from our measurements in 1D (see Fig. 2.5b). This computation yields:

$$\ell_H \approx 0.51 (\bar{A}_{1D} \sqrt{\phi_c})^{-2.78}. \quad (2.23)$$

We plot the 1D phase diagram in Fig. 2.11b, where the data are obtained in the same way as in 2D. The prediction is in good agreement with the data.

2.6 Discussion

We have proposed and demonstrated a simple method for obtaining homogeneous distributions of particles in non-Brownian suspensions. The ingredients are extremely simple: we take advantage of a density mismatch between the particles and the fluid that is common in real settings, plus cyclic shear flow. This protocol could be used to ease processing demands in applications. Of course, there are other means for evenly distributing particles in a fluid; chaotic advection has recently been proposed as another route for homogenizing a suspension [68]. The key advantage of our method is that the driving amplitude does not have to be set to a specific critical value. More broadly, we have shown that even in the presence of body forces on the particles, local collisions are sufficient to reach and maintain a homogenous state with hyperuniform scaling.

Looking beyond rheological behaviors, hyperuniform distributions of scattering sites can endow disordered colloidal suspensions with isotropic photonic band gaps [69, 70]. Our method could be used to prepare bulk materials with such optical properties, without the need to fine-tune the driving [54]. Moreover, by changing the driving amplitude, the mean particle spacing can be varied continuously while maintaining a hyperuniform state.

Surprisingly, our work has revealed three distinct combinations of the parameters κ , v_s , ϕ_c , and D that control self-organization in this system. The criteria for obtaining the critical density is set by the dimensionless parameter $\bar{A} \propto \kappa v_s / \phi_c D$, vertical density gradients scale with $\kappa v_s^2 / D^2$, and hyperuniformity is controlled by $\bar{A} \sqrt{\phi_c} \propto \kappa v_s / \sqrt{\phi_c} D$. By considering the interplay between these effects, we have identified an emergent lengthscale ℓ_H above which hyperuniform scaling breaks down. This lengthscale, arising from a competition between local organization and large-scale gradients, is sufficiently general that it should arise in other systems

with different driving.

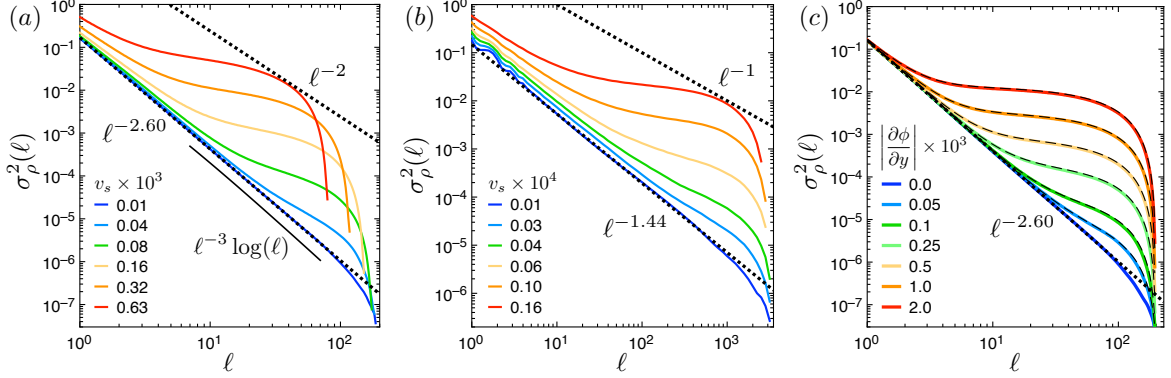


FIGURE 2.5: Number density fluctuations. **(a)** Steady-state variance of the number density, σ_ρ^2 , versus window size, ℓ , in 2D simulations with sedimentation and shear. The variance is calculated by measuring the number density of particle centers, ρ , in circular windows of diameter ℓ sampled uniformly throughout the suspension. Each curve is an average of 50 systems with $N = 9677$, $\gamma = 3.0$, and $\kappa = 48.4$. At low sedimentation speed, hyperuniform density fluctuations are observed, as shown by the dotted line following $0.17\ell^{-2.60}$. The data are also consistent with a larger exponent with a logarithmic correction: $\ell^{-3} \log(\ell)$ (solid line). An uncorrelated system would follow a scaling of ℓ^{-2} . **(b)** Analogous results in 1D simulations, averaged over 20 systems with $N = 3000$ and $\gamma = 1$. At low sedimentation speed, hyperuniform density fluctuations are observed over 3 decades in ℓ , following $0.15\ell^{-1.44}$. An uncorrelated system would follow a scaling of ℓ^{-1} . **(c)** Variance of the number density for initially hyperuniform 2D systems that were scaled along the y axis to impose a constant density gradient, $|\partial\phi/\partial y|$. Each curve is an average over 31 systems with $N = 10186$, $\gamma = 3.01$, $L = 200$, and $\phi = 0.2$. The variance increases with the size of the gradient. The data are precisely captured by summing the measurement at zero gradient with a term due to a uniform gradient that we calculate in the continuum limit (dashed lines: Eq. ?? computed with the value of $|\partial\phi/\partial y|$ in the legend).

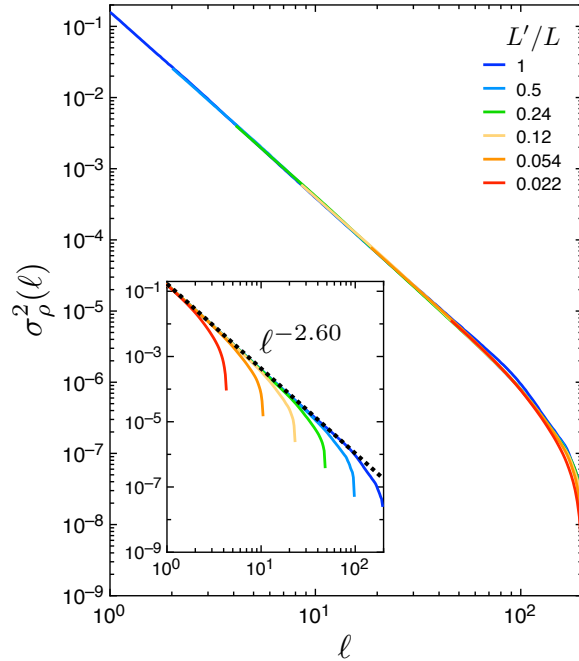


FIGURE 2.6: **Effect of system size on variance of the number density.** *Inset:* Variance of the number density, σ_ρ^2 , versus ℓ for a square system of size $L = 200$ and subsystems of size $L' < L$. The largest system has $N = 10186$, $\phi = 0.2$, and is sheared cyclically at amplitude $\gamma = 3.01 \approx \gamma_c$ until it reaches a reversible state. We thus obtain a hyperuniform configuration with a scaling exponent $\lambda = 2.60$. *Main:* We shift the curves by scaling the x axis by L/L' and y axis by $(L/L')^\lambda$. The data collapse onto a single master curve, which falls off rapidly when ℓL .

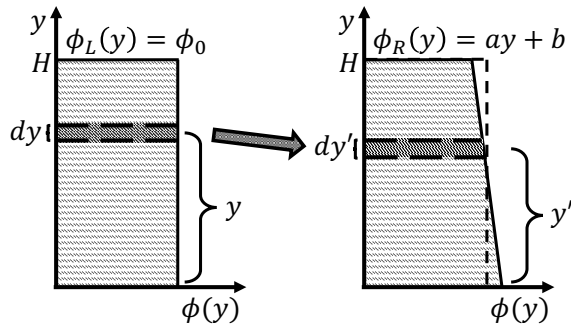


FIGURE 2.7: **Mapping a constant-density profile to a profile with a constant vertical gradient.** *Left:* Density profile, $\phi_L(y)$, versus vertical position, y (where the dependent variable is on the x axis so that vertical axis is oriented as in the simulation). The system has a uniform distribution along the y axis with a constant area fraction ϕ_0 . *Right:* Target density profile of the form $\phi_R(y) = ay + b$. The shaded region at position y with thickness dy is mapped to position y' with thickness dy' that conserves its mass.

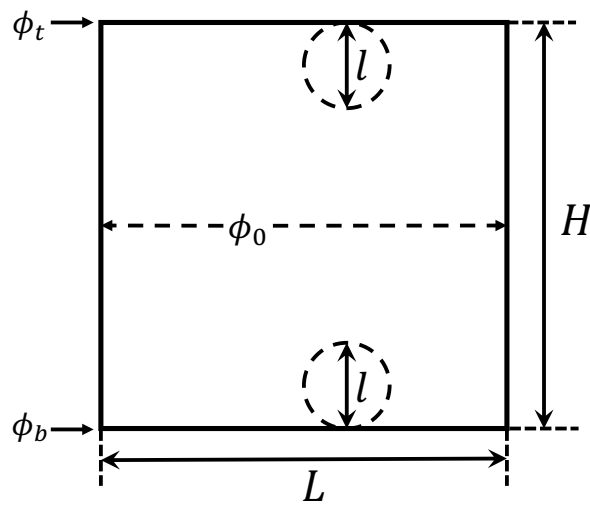


FIGURE 2.8: **Calculation of variance in system with constant vertical density gradient** A box of height H and width L contains a continuous density field $\phi(y)$. The system has a constant vertical density gradient $\partial\phi/\partial y$ and densities ϕ_t and ϕ_b at the top and bottom boundaries, respectively. The variance of the number density $\sigma_p^2(\ell)$ is calculated by measuring the mean density in circular regions of diameter ℓ , sampled uniformly throughout the region.

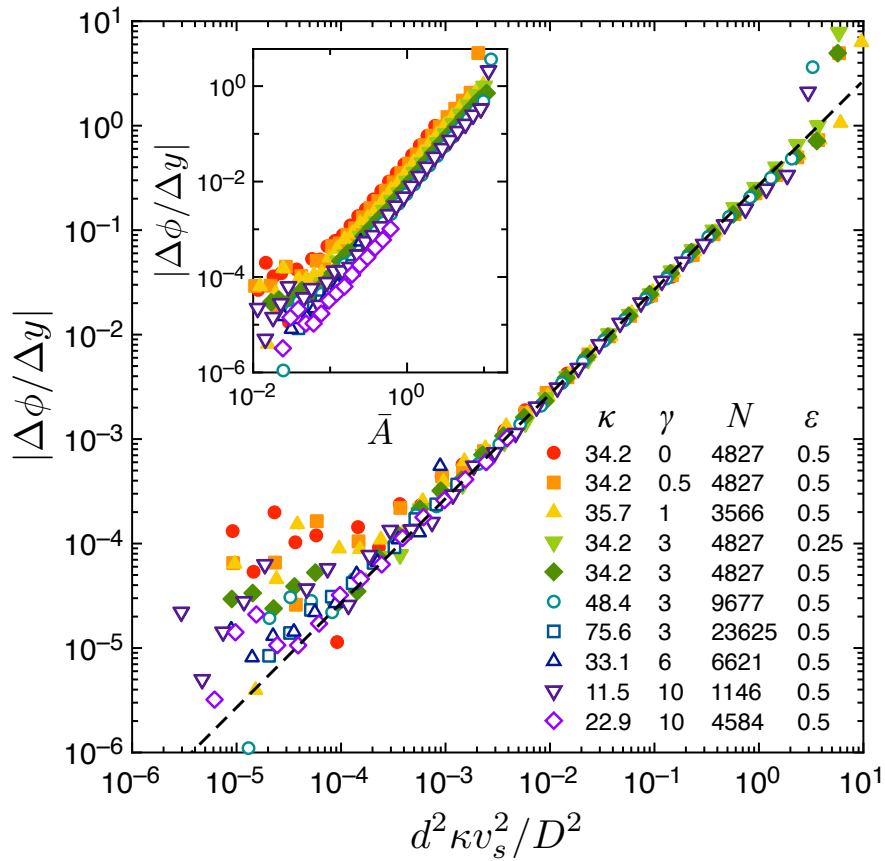


FIGURE 2.9: **Steady-state vertical density gradient.** $|\Delta\phi/\Delta y|$ versus $d^2\kappa v_s^2/D^2$ (main) and versus \bar{A} (inset). Data are from fitting the density profile of the middle 60% of the particles, averaging over 5 systems for each point. Dashed line: Scaling argument with fitted numerical prefactor, Eq. 2.17.

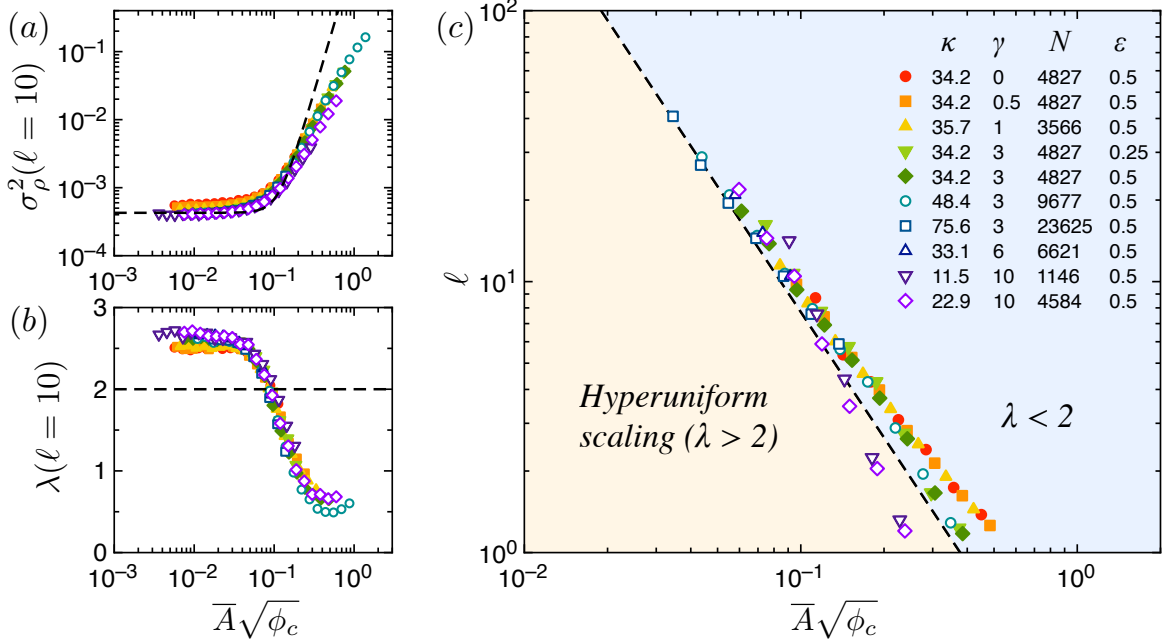


FIGURE 2.10: **Self-organized hyperuniformity.** (a) Variance of the number density, σ_ρ^2 , for sampling windows of size $\ell = 10$. The data over a wide range of parameters are collapsed when plotted versus $\bar{A}\sqrt{\phi_c}$. At low velocity (i.e., low $\bar{A}\sqrt{\phi_c}$), the data plateau to the value in the critical state. The increase at moderate velocities is well captured by Eq. 2.18 (dashed line) for the effect of vertical density gradients. (b) Magnitude of the local scaling exponent, λ , measured at $\ell = 10$. Hyperuniform scaling ($\lambda > 2$) is observed for $\bar{A}\sqrt{\phi_c} < 0.08$ at this lengthscale. (c) Phase diagram for hyperuniform density fluctuations. Hyperuniformity emerges below a finite threshold value of $\bar{A}\sqrt{\phi_c}$, and it extends to longer lengthscales as the control parameter $\bar{A}\sqrt{\phi_c}$ decreases. Symbols: Lengthscale ℓ_H where the local scaling exponent λ of the variance $\sigma_\rho^2(\ell)$ is shallower than 2. Dashed line: Phase boundary from our theory with no free parameters, Eq. 2.19.

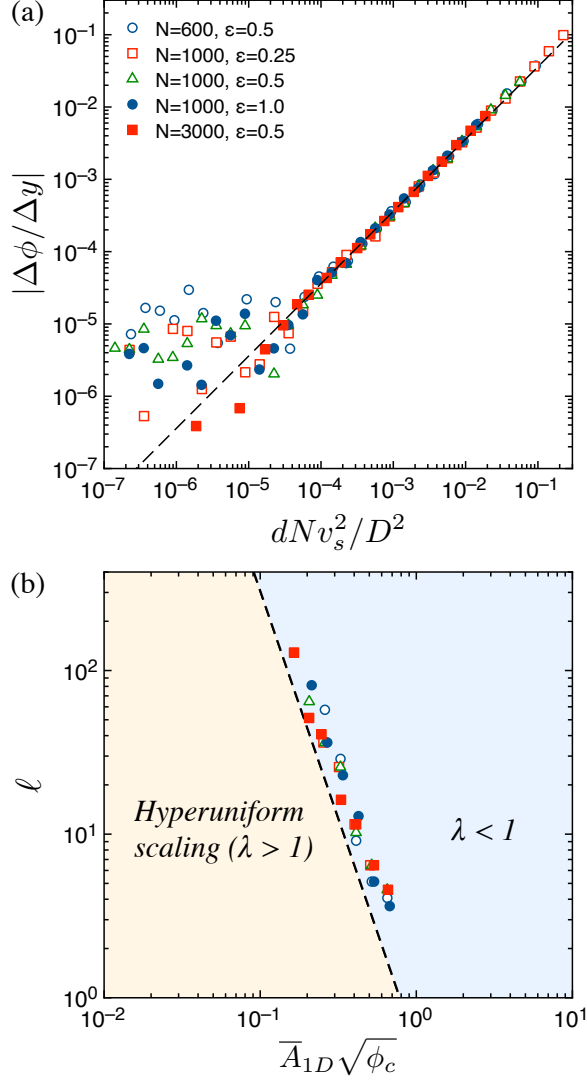


FIGURE 2.11: **One-dimensional model results.** (a) Magnitude of the vertical density gradient, $|\Delta\phi/\Delta y|$ versus dNv_s^2/D^2 , in the steady state. Data are from fits to the middle 60% of the density profile, averaged over 20 systems. Dashed line: Predicted scaling, Eq. 2.21. (b) Phase diagram. Symbols: Lengthscale ℓ_H where the local scaling exponent λ of the variance $\sigma_\rho^2(\ell)$ is shallower than 1. As in our 2D systems, we measure the variance over the bottom 99% of particles, and we consider windows of size $\ell < h_\infty/5$ to avoid system size effects. Dashed line: Phase boundary from our theory with no free parameters, Eq. 2.23. As in 2D, hyperuniform scaling emerges below a finite threshold value of $\overline{A}\sqrt{\phi_c}$ and extends to longer lengthscales at smaller $\overline{A}\sqrt{\phi_c}$.

Chapter 3

Self-organized compaction fronts in cyclically-sheared sinking grains

This chapter is based on a manuscript being prepared for submission with J. M. Schwarz and J. D. Paulsen as co-authors. My contribution was to write original simulation code, perform and analyze the simulations, and contribute to the discussion of the results and the writing of the manuscript.

3.1 Background

At thermal equilibrium, the interface separating two coexisting phases is diffuse: the composition varies continuously from one phase to the other over a finite length. Recent experiments on dynamic jamming fronts in two dimensions [1] identified a diffuse interface between the jammed and unjammed discs. In both cases, the thickness of the interface diverges as a critical transition is approached. Noting this similarity, we investigate the generality of such interfaces using a third system: random organization in a model of cyclically-sheared non-Brownian suspensions. We sediment the particles towards a boundary to initiate traveling fronts between

an active irreversible phase and a quiescent reversible phase. The front width diverges as a critical concentration is approached, which we connect with a diverging lengthscale in the bulk.

When a collection of loose grains is impacted, a jammed region may develop that grows as it amasses more and more grains on its propagating boundary [71, 72]. Such dynamic jamming underlies the unsteady stress transmission in a wide range of settings, from iceberg-choked fjords [73] to water and cornstarch suspensions [74–76]. Jamming fronts are also present at low strain rates in the sedimentation of suspensions, as particles accumulate at the interface marking the top of the sediment [77, 78]. Understanding the response of such disordered systems driven far from equilibrium continues to be a frontier of soft-matter science [79].

3.1.1 Dynamical jamming front

Recent experiments by Waitukaitis *et al.* [44] found that the interface between the dynamically jammed mass and its quiescent surroundings may be surprisingly thick. They observed a finite front width that diverged as the dilute phase approaches the jamming density, which they rationalized by appealing to a diverging correlation length at the jamming point [80–83]. The width of such fronts is important because it influences when the growing phase starts to interact with other boundaries or obstacles. However, it was not clear whether their arguments could translate to other settings, to serve as an organizing principle among other nonequilibrium systems.

3.2 Sedimenting suspensions

Here, we show how to obtain propagating fronts in another system falling in a distinct universality class. We study random organization in a simplified model of non-Brownian particles under cyclic shear [30]. By sedimenting the particles into a hard boundary [39, 84], we create a propagating interface between irreversible and reversible regions in the suspension (Fig. 3.1b). We show that the front width diverges as the dilute phase approaches the critical density, as was found in the jamming scenario [44]. We then link the interface thickness to a bulk correlation length by measuring a growing correlation length in systems without sedimentation. Unlike in the jamming scenario, the dense phase is mobile with an effective diffusion constant, whose magnitude surprisingly does not affect the front width. Our results reveal qualitative connections between dynamic interfaces in jamming and random organization, as well as static interfaces in equilibrium systems near criticality.

3.2.1 Model

Our simulations are based on a simplified model of cyclically-sheared suspensions proposed by Corté *et al.* [30]. We use a zero-shear version of the model [55], which has the same qualitative behaviors as for finite shear. The model evolves the dynamics of N discs of diameter $d = 1$ in a box of area L^2 using discrete cycles, where particles that overlap during a cycle are given a small kick in a random direction (Fig. 3.1a), with a magnitude chosen uniformly between 0 and a fixed maximum kick size, ϵ . For small area fractions $\phi_0 = N\pi/(4L^2)$, the particles eventually self-organize into one of many random absorbing states, where there are no overlaps and the dynamics is reversible thereafter. Previous work identified a critical transition at a density ϕ_c , so that for $\phi_0 > \phi_c$ the steady state is irreversible and the

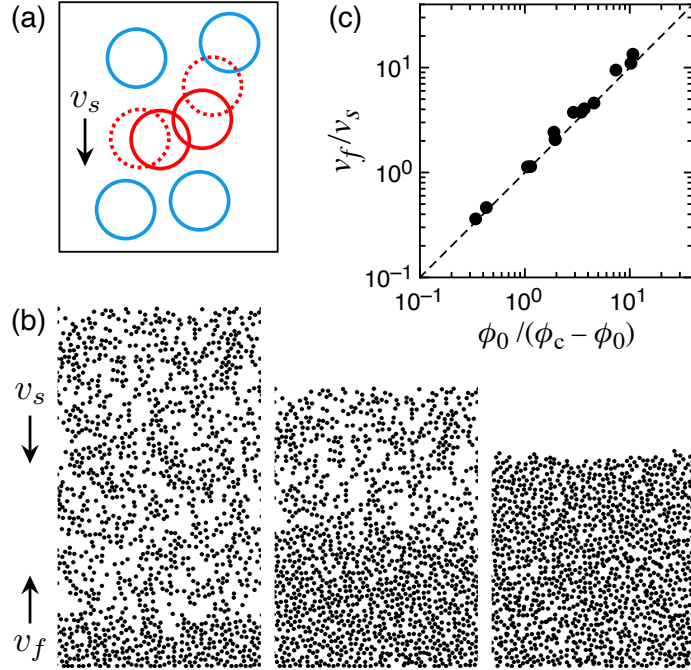


FIGURE 3.1: **Self-organized compaction front.** (a) Simplified model of a cyclically-sheared suspension after Ref. [30]. In each cycle, a uniform sedimentation velocity v_s is applied to all particles, and particles that overlap (red) are given random kicks, to simulate local irreversibility due to collisions. (b) In the simulations, a dense region grows upwards with a front velocity v_f . When the front reaches the top of the system, a steady state is attained. (c) Scaled front velocity, v_f/v_s . Dashed line: Theoretical prediction [Eq. (3.1)], which assumes that the dilute and dense phases have uniform densities equal to ϕ_0 and ϕ_c (measured independently). Parameter ranges: $0.05 \leq \epsilon \leq 10$, $300 < N < 16300$, $10^{-6} \leq v_s \leq 4 \times 10^{-4}$, $0.05 \leq \phi_0 \leq 0.40$, $0.15 \leq \phi_0 \leq 0.44$.

dynamics is diffusive at long times [30, 85].

Significant effort has been devoted to understanding the behaviors of this model under uniform initial conditions and driving [52, 59, 61, 86–88]. Here we probe the transient dynamics under the addition of slow sedimentation. Following Refs. [39, 84], each cycle in our simulations has an additional component in which all particles are displaced downwards by a uniform amount, v_s . To capture collisions with the bottom wall, all particle centers with $y < d/2$ are reflected about that line at the end of each cycle. We apply periodic boundary conditions to the side walls. We study a

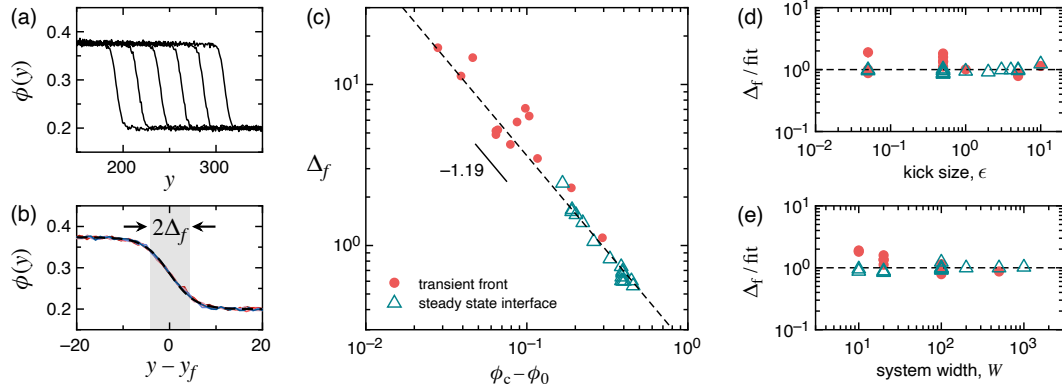


FIGURE 3.2: **Interface shape and thickness.** (a) Density profile snapshots, spaced evenly in time. The system has $\epsilon = 0.5$, $v_s = 1.7 \times 10^{-5}$, $\phi_0 = 0.2$, $\phi_c = 0.376$. Translating these 6 profiles atop one another shows that the front propagates with a fixed shape and width. The measured profile is consistent with a sigmoid function (dashed line). We fit this function to the data to measure the front width, Δ_f , for each simulation. (c) Measured front width, Δ_f , versus distance to criticality of the sedimenting phase, $\phi_c - \phi_0$. Closed symbols: transient fronts. Open symbols: interface at the top of the system in the steady state (where ϕ_0 is therefore taken to be zero). The data at sufficiently small $\phi_c - \phi_0$ are consistent with a power-law with exponent -1.20 ± 0.15 (dashed line). (d,e) To test for any dependence on other system parameters, we divide the data by the power-law fit in panel (c). The behavior shows no trend with kick size, ϵ . There is also no growth of the front width with the system width, which would occur if the interface were rough. Parameter ranges in (c-e): $0.05 \leq \epsilon \leq 10$, $300 < N < 8600$, $10^{-7} \leq v_s \leq 4 \times 10^{-4}$, $0.05 \leq \phi_0 \leq 0.40$, $0.15 \leq \phi_c \leq 0.44$.

regime at low sedimentation speed, where the timescale for sedimentation is longer than the timescale for diffusion: $v_s \ll 16\phi_c DL / (\pi d^2 N)$, where D is the coefficient of diffusion for a non-sedimenting system measured at $\phi = 2\phi_c$.

Figure 3.1b shows a typical system evolution. In the steady state (rightmost image), the particles settle into a column with an approximately constant density that is very near ϕ_c , as was shown before [39, 84]. Here we see that the system reaches this state by a front that moves upwards through the system, separating a compacted region from a dilute region. Each simulation setting has been simulated 200 to 400 times for averaging to acquire quality results for plotting.

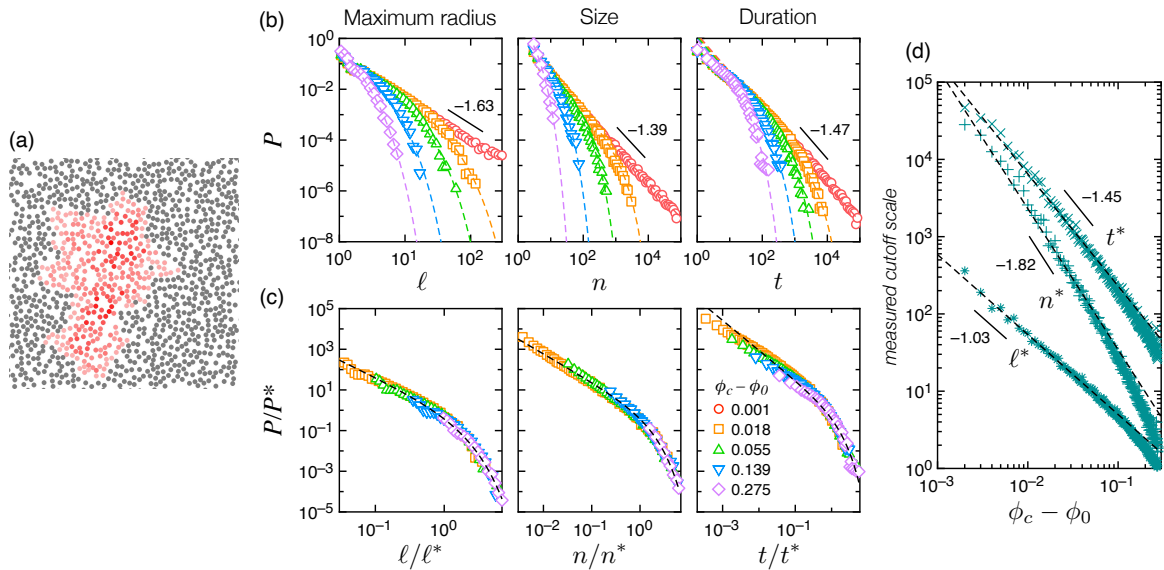


FIGURE 3.3: **Response to point perturbation.** (a) Starting from a quiescent state, a perturbation may set off a chain reaction in which many particles are activated before the system becomes quiescent again. The red particles were active at some time during the avalanche; darker particles received more total kicks. (b) Histograms collected over many systems for the distance to the farthest activated particle, ℓ , the number of activated particles, n , and the avalanche duration in cycles, t . Solid lines: Fits to Eq. (3.7), where the measured exponent α is indicated in each panel. (c) The curves are approximately collapsed when scaled by the position of the exponential cutoff. (d) Value of the cutoff versus $\phi_c - \phi_0$. Each curve diverges as a power law, with another exponent that is distinct from α (see Table 3.1). All data are for $\epsilon = 0.5$ and $L = 400$.

3.2.2 Front velocity and particle conservation

If we assume that the dilute region has constant density ϕ_0 and the sediment has constant density ϕ_c , then conservation of area dictates [78]:

$$v_s \phi_0 = v_f (\phi_c - \phi_0), \quad (3.1)$$

where v_f is the speed of the front. We compare this prediction with the measured v_f in Fig. 3.1c, where we obtain ϕ_c from independent simulations without sedimentation that otherwise matches the conditions of the particular data point (e.g., same

N, L, ϵ . We find very good agreement, validating this straightforward picture for the front velocity.

These considerations do not constrain the front profile. Figure 3.2a shows the density profile from a typical simulation at equal intervals in time. Shifting the curves onto one another, we find that the front shape is invariant in time (Fig. 3.2b). It could be consistent with a sigmoid or an error function.

3.2.3 Derivation of the front profile

Assuming that front has already formed and has a profile of the hyperbolic tangent function. We also assume that, at packing fraction ϕ , the chance of the existing active cluster of particles stopping is

$$p(\phi) = \frac{1}{\phi_c - \phi} \quad (3.2)$$

Then, we can calculate the probability distribution of where would an incoming active cluster of particles stop due to the lack of surrounding particles.

$$f(y) = p(\phi(x)) \prod_{-\infty}^y (1 - p(\phi(x))) \quad (3.3)$$

By calculating the derivative of the front profile function we can obtain the incremental change of density between cycles.

$$\frac{d\phi}{dy} = \frac{\phi_c - \phi}{\Delta y} \left(e^{\frac{y_f - y}{\Delta y}} + e^{\frac{y - y_f}{\Delta y}} \right)^{-1} \quad (3.4)$$

We measure the front width by fitting the profile to the function:

$$\phi(y) = \phi_2 - \frac{\phi_2 - \phi_1}{1 + e^{(y - y_f)/\Delta_f}} \quad (3.5)$$

Note that the densities ϕ_1 , ϕ_2 represent the measured density plateaus and may differ slightly from ϕ_c and ϕ_0 . We fit them to the data to ensure that Δ_f corresponds to the interface thickness and is not influenced by variations in these quantities.

Noting that the particles are diffusive in the sediment, one may expect the kick size ϵ to affect the front width, since larger ϵ leads to a larger effective diffusion constant, D . Surprisingly, we find the front width to be independent of ϵ in our simulations. Instead, we find that the front width depends on $\phi_c - \phi_0$ alone, as shown in Fig. 3.2c. We can find the same behavior in the steady state, by measuring the thickness of the interface at the top of the system, where in this case ϕ_0 is taken to be zero. These data are plotted as open symbols in Fig. 3.2c. Altogether, the data are consistent with a power law:

$$\Delta_f \propto (\phi_c - \phi_0)^{-\beta}. \quad (3.6)$$

with $\beta = 1.19 \pm 0.13$. Note that ϕ_c and ϕ_0 are already determined for these data in the same manner as Fig. 3.1c, so that the uncertainty is due to the scatter in the data.

To test this picture further, Fig. 3.2(d,e) shows the same data where we now divide the measured Δ_f by Eq. 3.6. Plotting the results as a function of ϵ , we confirm that the interface thickness shows no trend with kick size. Plotting the results as a function of W indicates that the interface is not rough [89], as Δ_f does not systematically increase with system width, W .

3.3 Correlation lengthscale

A finite interface thickness observed in dynamic jamming fronts was explained by appealing to a diverging correlation lengthscale on approach to jamming [44]. For random organization, diverging lengthscales have been reported with exponents

		Expression	DP	CDP/Manna	Present work
Decay	Maximum radius	$2\tau - 1$	1.536	1.560	1.63 ± 0.10
	Size	τ	1.268	1.280	1.39 ± 0.07
	Duration	τ_t	1.450	1.510	1.47 ± 0.09
Cutoff	Maximum radius, ℓ^*	$1/(2\sigma)$	1.089	1.115	1.03 ± 0.08
	Size, n^*	$1/\sigma$	2.179	2.229	1.82 ± 0.20
	Duration, t^*	$1/\sigma_t$	1.297	1.225	1.45 ± 0.14

TABLE 3.1: **Comparison of critical exponents.** Values are shown for directed percolation (DP, obtained from Ref. [34]), conserved directed percolation (CDP/Manna, obtained from Ref. [35]) and the present work using point perturbations in the isotropic random organization model. Greek notation matches that of Ref. [34].

ranging from 0.72 to 1.1. In particular, Tjhung and Berthier [61] reported static and dynamic lengthscales with exponents of 0.73 ± 0.04 and 0.77 ± 0.06 respectively, and a hyperuniform lengthscale with exponent 0.76 or 1.23 when approaching ϕ_c from below or above, respectively [55]. Hexner and Levine reported a hyperuniform lengthscale with an exponent 0.8 for noiseless systems [54] and 1.1 ± 0.1 when noise is present [88]. However, it is not a priori clear which of these exponents might be related to the diverging front width that we observe.

3.3.1 Point perturbation

One intuitive method to probe a diverging lengthscale is to perturb the system at a point and measure the characteristic radius of the region that responds, as was done for the jamming transition [81]. This approach is appealing for the problem at hand, where the front marks the top surface of the active region at ϕ_c where particles are continually activated, causing further activations to propagate up through the dilute region at density ϕ_0 . In our regime at low sedimentation velocities, the thickness of the interface may correspond to the maximum vertical extent of these avalanches.

To study the response to a point perturbation, we start by initializing systems at some $\phi_0 < \phi_c$ in a square box of side $L = 400$, and evolve them to a reversible state in the absence of sedimentation. Then, we give one particle a random kick. We again evolve the system to a reversible state. Figure 3.3a shows an example where the colored particles were active at some time during the avalanche. (Initial positions shown? Final positions?) For each avalanche, we measure the distance (initial? Final?) to the farthest particle that is activated, ℓ , the total number of particles that are activated, n , and the duration of the avalanche in cycles, t . If no other particles are activated, this corresponds to $\ell = 0$, $n = 0$, and $t = 0$.

3.4 Universality class

3.4.1 Calculation of scaling exponents

To build up statistics, for each value of ϕ_0 , we generate up to 100 reversible states as the initial states for the perturbation; each is used in 1,000 tests where we select one particle at random, give it a random kick, and observe the resulting avalanche. Histograms of these quantities are shown in Fig. 3.3b, for five different values of $\phi_c - \phi_0$, all with $\epsilon = 0.5$. We find good fits to the function:

$$P(x) \propto x^{-\alpha} \exp(-x/x^*), \quad (3.7)$$

where α is determined by fitting a power law to the curve that is closest to the critical state, and then A , x^* are fit for each curve. The data may be collapsed onto a master curve (Fig. 3.3c). We find good collapses for the histograms of ℓ and n but not as good for t , as the data for $t \geq 10$ are not as steep and thus peel off the collapse.

Although data for only five densities are shown in Fig. 3.3b,c for illustration, in total we generate histograms at over 200 distinct values of $\phi_c - \phi_0$, and we fit Eq. 3.7 to each of them. Our measurements of ℓ^* , n^* , and t^* are shown in Fig. 3.3d. Each diverges with a different exponent.

3.4.2 Compared with DP and CDP

Together with Fig. 3.3b, we measure six exponents from these data, which we list in Table 3.1. The values could be consistent with the directed percolation universality class or conserved directed percolation. Of particular interest is ℓ^* , which signifies the largest radial extent of a ‘typical’ avalanche. We propose it is central to setting the interface thickness in the sedimenting suspensions. We measure the exponent to be 1.03 ± 0.08 , consistent with the measured exponent for the interface thickness in the sedimentation simulations, 1.19 ± 0.13 (Fig. 3.2c).

Such comparisons of exponents have been made previously [30, 55, 61, 86], but the exponent $1/(2\sigma)$ from DP or CDP had not been identified as controlling a lengthscale in random organization, as we have shown here. It may correspond to the exponent for the lengthscale ξ_2 in Ref. [88], for which they measured an exponent of 1.1 ± 0.1 in the Manna model.

3.5 Discussion

Whereas Young and Laplace conceived of fluid interfaces as zero-thickness surfaces, it is now understood that physical properties make rapid but smooth transitions there [90]. The finite thickness of an equilibrium fluid interface becomes most apparent near a critical point, where the interface becomes more and more diffuse and its thickness diverges [91–93]. Here, we observed an interface between

reversible and irreversible phases in a model of a cyclically-sheared suspension, and we demonstrated the divergence of its thickness in the vicinity of a nonequilibrium critical point.

Several properties of the interface place it in contrast with other non-equilibrium systems. The front widths we observe are invariant in time, unlike many interfacial growth phenomena captured by Poisson-like growth or the Kardar-Parisi-Zhang universality class [89, 94, 95]. Our interfaces are also not observed to roughen, unlike in the two-dimensional Ising model [96]. Instead, our interfaces bear a stronger qualitative resemblance to an equilibrium fluid near a critical point, where a diverging bulk lengthscale is likewise associated with the diverging interface thickness [93].

We have also identified strong similarities with the phenomenology of dynamic jamming fronts [44]. Relationships between random organization and jamming have been explored in the past by developing simple models that can interpolate between these two possible limiting behaviors of particulate systems with random or deterministic pairwise interactions [85, 97]. Here we unified a particular phenomenology in these systems by comparing results from previous dynamic jamming experiments [44] and our simulations of random organization. We propose that the essential shared features are (i) a critical transition, and (ii) a mechanism for driving the system from a dilute phase towards a dense phase that has an upper limit on its density. Here we have shown that slow sedimentation [39, 84] provides such a route for random organization. The connection is perhaps surprising as there is a nonlinear diffusion process in random organization, which one might expect would further broaden the fronts. We have shown that it does not. Yet, this nonlinear diffusion process offers a potentially useful feature: the critical phase of

a cyclically-sheared suspension may be continuously varied by changing the driving amplitude, allowing some control over the dense phase that is not available in jamming.

Chapter 4

Conclusion

4.1 Summary

Thank you for reading through my thesis and here is a summary of what I and my advisors did in the past years and what we have learned from it. We first learned the concept of hyperuniformity which, at that time, was a novel and emerging topic that captured many researchers' attention. Joey proposed the idea of sedimentation and suggested we find hyperuniformity in a sheared sedimenting suspensions. We conducted simulations based on Corté's model and performed statistical analysis on data. We then found reduced large scale spatial density variations (hyperuniformity) and further confirmed it via examination of structural factors. Because of the nature of sedimentation, there exists a density gradient that interferes with generating hyperuniform suspensions. Thus, we derived a theoretical model to directly predict the point at which the system loses hyperuniformity. More importantly, we quantified the necessary system conditions and preparation time to achieve hyperuniformity in a sheared sedimenting system. After getting familiar with inhomogeneous suspensions, we proceed to explore more properties is such a system. Inspired by dynamical jamming fronts [1], we focused on researches of a similar compaction front that has been discovered in our system. The propagating front

shows up when suspensions start to sediment and disappears when the suspension is in steady state. We found the hyperbolic function is a good match to the density profile of the transitional front. The width of the front was verified only depends on the difference of packing fraction of two separate sides while not relate to other system parameters. This surprised us for its counter-intuitive phenomenon and revealed the intrinsic behavior of sheared suspensions. This may indicate that the geometry of such a system can be invariant even with different dynamical properties of the system. We continued to acquire information of the corresponding homogeneous system to be compared with compaction fronts. We performed single point perturbation to the system and measured various quantities including max reach of a perturbed active cluster, cluster size, and duration of the cluster. Thus, we can compare the scaling of different realizations of suspensions and eventually compare them to the universality class of DP and CDP.

4.2 Future works

Although I have spent some quality time researching the self-organization of disordered systems. There are still some unfinished work or interesting directions that can be further studied for the best.

4.2.1 Hyperuniformity in higher dimension

Since our work is entirely based on 2D suspensions, we were always wondering if there exists hyperuniformity in 3D sedimenting suspensions. Using simulation scripts based on Corté's model, it's not hard to implement a 2D system with enough particles to utilize. When encountered with a higher dimension system, the simulation model will require significantly increased computing workloads. This can

be optimized via updating the model, improve the algorithm, or using better hardware like GPUs or distributive computing facilities. We currently have little idea of higher-dimensional hyperuniformity and this research could be quite helpful for us to understand it in a more abstract way.

4.2.2 Hyperuniformity in networks

With the knowledge of hyperuniformity of higher dimensions, we can further our reach to networks. Like the force network that people construct in a jammed system, we can also construct a probabilistic network that connects particles in a loosely packed system. This enables us to borrow powerful analytical tools from graph theory to analyze a hyperuniform system and compare it to a typical disordered system. Thus, we can have a new way of measuring hyperuniformity and, more importantly, a perspective of hyperuniformity in networks. Modern networks include neural networks, traffic networks, logistic networks, social networks and so much more. The unique features of a hyperuniform network could lead us to a deeper understanding of nature and its principles.

4.2.3 Robustness of hyperuniform networks

A neural network in the human brain is designed to perform sophisticated tasks and, at the same time, to be robust to improve our chance to survive in a rapidly changing environment. It's proven that a hyperuniform system will contain less amount of information with the same amount of media compared to a random system. This could have its unique value in various applications. Our brain may utilize this redundant structure to accommodate damages in our neural network. When developing machine learning models, applying the mechanism of random organization may suppress overfitting and improve validation scores.

Bibliography

- ¹S. R. Waitukaitis, L. K. Roth, V Vitelli, and H. M. Jaeger, “Dynamic jamming fronts”, English, *EPL (Europhysics Letters)* **102**, 44001 (2013).
- ²V. F. Hagh, E. I. Corwin, K. Stephenson, and M. F. Thorpe, “A broader view on jamming: from spring networks to circle packings”, *Soft Matter* **15**, 3076–3084 (2019).
- ³D. SEMWOGERERE, J. F. MORRIS, and E. R. WEEKS, “Development of particle migration in pressure-driven flow of a brownian suspension”, *Journal of Fluid Mechanics* **581**, 437–451 (2007).
- ⁴G. J. Klir and W. R. Ashby, “Facets of systems science”, 521–536 (1991).
- ⁵R. Wedlich-Söldner and T. Betz, “Self-organization: the fundament of cell biology”, *Philosophical Transactions of the Royal Society B: Biological Sciences* **373**, 20170103 (2018).
- ⁶J. Duran, “Sands, Powders, and Grains, An Introduction to the Physics of Granular Materials”, *Partially Ordered Systems*, 10.1007/978-1-4612-0499-2 (2000).
- ⁷H. Tsoar, “Bagnold, r.a. 1941: the physics of blown sand and desert dunes. london: methuen”, *Progress in Physical Geography: Earth and Environment* **18**, 91–96 (1994).
- ⁸G. Oron and H. Herrmann, “Contact forces in regular 3D granular pile”, *Physica A: Statistical Mechanics and its Applications* **265**, 455–462 (1999).

- ⁹F. Nicot, “Constitutive modelling of snow as a cohesive-granular material”, *Granular Matter* **6**, 47–60 (2004).
- ¹⁰H. M. JAEGER and S. R. NAGEL, “Physics of the Granular State”, *Science* **255**, 1523–1531 (1992).
- ¹¹H. M. Jaeger, S. R. Nagel, and R. P. Behringer, “Granular solids, liquids, and gases”, *Reviews of Modern Physics* **68**, 1259–1273 (1996).
- ¹²I. Zuriguel, A. Garcimartín, D. Maza, L. A. Pugnaloni, and J. M. Pastor, “Jamming during the discharge of granular matter from a silo”, *arXiv*, 10.1103/physreve.71.051303 (2004).
- ¹³R. P. Behringer, “Jamming in granular materials”, *Comptes Rendus Physique* **16**, 10–25 (2015).
- ¹⁴D. Bi, J. Zhang, B. Chakraborty, and R. P. Behringer, “Jamming by shear”, *Nature* **480**, 355–358 (2011).
- ¹⁵C. P. Goodrich, W. G. Ellenbroek, and A. J. Liu, “Stability of jammed packings i: the rigidity length scale”, *Soft Matter* **9**, 10993–10999 (2013).
- ¹⁶S. Papanikolaou, C. S. O’Hern, and M. D. Shattuck, “Isostaticity at frictional jamming”, *Phys. Rev. Lett.* **110**, 198002 (2013).
- ¹⁷J Schäfer, S Dippel, and D. E. Wolf, “Force schemes in simulations of granular materials”, *Journal de Physique I* **6**, 5–20 (1996).
- ¹⁸S. Torquato and F. H. Stillinger, “Jammed hard-particle packings: from kepler to bernal and beyond”, *Rev. Mod. Phys.* **82**, 2633–2672 (2010).
- ¹⁹A. J. Liu and S. R. Nagel, “Jamming is not just cool any more”, *Nature* **396**, 21–22 (1998).

- ²⁰C. S. O'Hern, L. E. Silbert, A. J. Liu, and S. R. Nagel, "Jamming at zero temperature and zero applied stress: the epitome of disorder", *Physical Review E* **68**, 011306 (2003).
- ²¹M. v. Hecke, "Jamming of soft particles: geometry, mechanics, scaling and isotaticity", *Journal of Physics: Condensed Matter* **22**, 033101 (2010).
- ²²S. F. Edwards and D. V. Grinev, "Statistical mechanics of stress transmission in disordered granular arrays", *Physical Review Letters* **82**, 5397–5400 (1999).
- ²³T. S. Majmudar and R. P. Behringer, "Contact force measurements and stress-induced anisotropy in granular materials", *Nature* **435**, 1079–1082 (2005).
- ²⁴C. Song, P. Wang, and H. A. Makse, "A phase diagram for jammed matter", *Nature* **453**, 629–632 (2008).
- ²⁵L. E. Silbert, D. Ertaş, G. S. Grest, T. C. Halsey, and D. Levine, "Geometry of frictionless and frictional sphere packings", *Physical Review E* **65**, 031304 (2002).
- ²⁶S. Henkes, M. v. Hecke, and W. v. Saarloos, "Critical jamming of frictional grains in the generalized isostaticity picture", *EPL* **90**, 14003 (2010).
- ²⁷L. E. Silbert, "Jamming of frictional spheres and random loose packing", *Soft Matter* **6**, 2918–2924 (2010).
- ²⁸N. Kumar and S. Luding, "Memory of jamming—multiscale models for soft and granular matter", *Granular Matter* **18**, 58 (2016).
- ²⁹D. J. Pine, J. P. Gollub, J. F. Brady, and A. M. Leshansky, "Chaos and threshold for irreversibility in sheared suspensions", *Nature* **438**, 997–1000 (2005).
- ³⁰L. Corte, P. M. Chaikin, J. P. Gollub, and D. J. Pine, "Random organization in periodically driven systems", *Nat. Phys.* **4**, 420 (2008).

- ³¹J. D. Paulsen, N. C. Keim, and S. R. Nagel, “Multiple transient memories in experiments on sheared non-brownian suspensions”, *Physical review letters* **113**, 068301 (2014).
- ³²H. Hinrichsen, “Non-equilibrium critical phenomena and phase transitions into absorbing states”, *Advances in Physics* **49**, 815–958 (2000).
- ³³G. Ódor, “Universality classes in nonequilibrium lattice systems”, *Reviews of Modern Physics* **76**, 663–724 (2004).
- ³⁴M. A. Muñoz, R. Dickman, A. Vespignani, and S. Zapperi, “Avalanche and spreading exponents in systems with absorbing states”, *Phys. Rev. E* **59**, 6175–6179 (1999).
- ³⁵S. Lübeck, “Universal scaling behavior of non-equilibrium phase transitions”, *International Journal of Modern Physics B* **18**, 3977–4118 (2004).
- ³⁶S. S. Manna, “Two-state model of self-organized criticality”, *Journal of Physics A: Mathematical and General* **24**, L363 (1999).
- ³⁷D. Hexner and D. Levine, “Noise, diffusion, and hyperuniformity”, *Phys. Rev. Lett.* **118**, 020601 (2017).
- ³⁸Y. Jiao, T. Lau, H. Hatzikirou, M. Meyer-Hermann, J. C. Corbo, and S. Torquato, “Avian photoreceptor patterns represent a disordered hyperuniform solution to a multiscale packing problem”, *Physical Review E* **89**, 022721 (2014).
- ³⁹L. Corté, S. J. Gerbode, W. Man, and D. J. Pine, “Self-organized criticality in sheared suspensions”, *Phys. Rev. Lett.* **103**, 248301 (2009).
- ⁴⁰Z. Ma and S. Torquato, “Random scalar fields and hyperuniformity”, *English, Journal of Applied Physics* **121**, 244904 (2017).
- ⁴¹S. Atkinson, G. Zhang, A. B. Hopkins, and S. Torquato, “Critical slowing down and hyperuniformity on approach to jamming”, *Phys. Rev. E* **94**, 012902 (2016).

- ⁴²G. Zhang, F. H. Stillinger, and S. Torquato, “The Perfect Glass Paradigm: Disordered Hyperuniform Glasses Down to Absolute Zero”, *Scientific Reports* **6**, 36963 (2016).
- ⁴³.
- ⁴⁴S. R. Waitukaitis, L. K. Roth, V. Vitelli, and H. M. Jaeger, “Dynamic jamming fronts”, *EPL (Europhysics Letters)* **102**, 44001 (2013).
- ⁴⁵J. Singh, A. E. Patteson, B. O. T. Maldonado, P. K. Purohit, and P. E. Arratia, “Bacterial activity hinders particle sedimentation”, *Soft Matter* **17**, 4151–4160 (2021).
- ⁴⁶J. Palacci, C. Cottin-Bizonne, C. Ybert, and L. Bocquet, “Sedimentation and effective temperature of active colloidal suspensions”, *Physical Review Letters* **105**, 088304 (2010).
- ⁴⁷N. J. Wagner and J. F. Brady, “Shear thickening in colloidal dispersions”, *Physics Today* **62**, 27–32 (2009).
- ⁴⁸E. Brown, N. A. Forman, C. S. Orellana, H. Zhang, B. W. Maynor, D. E. Betts, J. M. DeSimone, and H. M. Jaeger, “Generality of shear thickening in dense suspensions”, *Nature materials* **9**, 220–224 (2010).
- ⁴⁹X. Cheng, J. H. McCoy, J. N. Israelachvili, and I. Cohen, “Imaging the microscopic structure of shear thinning and thickening colloidal suspensions”, *Science* **333**, 1276–1279 (2011).
- ⁵⁰S. M. Fielding, P. Sollich, and M. E. Cates, “Aging and rheology in soft materials”, *Journal of Rheology* **44**, 323–369 (2000).
- ⁵¹P. Pham, B. Metzger, and J. E. Butler, “Particle dispersion in sheared suspensions: crucial role of solid-solid contacts”, *Physics of Fluids* **27**, 051701 (2015).

- ⁵²K. J. Schrenk and D. Frenkel, "Communication: evidence for non-ergodicity in quiescent states of periodically sheared suspensions", *The Journal of Chemical Physics* **143**, 241103 (2015).
- ⁵³A. Franceschini, E. Filippidi, E. Guazzelli, and D. J. Pine, "Transverse alignment of fibers in a periodically sheared suspension: an absorbing phase transition with a slowly varying control parameter", *Physical review letters* **107**, 250603 (2011).
- ⁵⁴D. Hexner and D. Levine, "Hyperuniformity of critical absorbing states", *Phys. Rev. Lett.* **114**, 110602 (2015).
- ⁵⁵E. Tjhung and L. Berthier, "Hyperuniform density fluctuations and diverging dynamic correlations in periodically driven colloidal suspensions", *Phys. Rev. Lett.* **114**, 148301 (2015).
- ⁵⁶S. Torquato and F. H. Stillinger, "Local density fluctuations, hyperuniformity, and order metrics", *Phys. Rev. E* **68**, 041113 (2003).
- ⁵⁷R. L. Jack, I. R. Thompson, and P. Sollich, "Hyperuniformity and phase separation in biased ensembles of trajectories for diffusive systems", *Physical review letters* **114**, 060601 (2015).
- ⁵⁸N. C. Keim and S. R. Nagel, "Generic transient memory formation in disordered systems with noise", *Physical review letters* **107**, 010603 (2011).
- ⁵⁹N. C. Keim, J. D. Paulsen, and S. R. Nagel, "Multiple transient memories in sheared suspensions: robustness, structure, and routes to plasticity", *Physical Review E* **88**, 032306 (2013).
- ⁶⁰P. Bak, C. Tang, and K. Wiesenfeld, "Self-organized criticality: an explanation of the 1/f noise", *Physical review letters* **59**, 381 (1987).

- ⁶¹E. Tjhung and L. Berthier, “Criticality and correlated dynamics at the irreversibility transition in periodically driven colloidal suspensions”, *Journal of Statistical Mechanics: Theory and Experiment* **2016**, 033501 (2016).
- ⁶²R. Dreyfus, Y. Xu, T. Still, L. A. Hough, A. Yodh, and S. Torquato, “Diagnosing hyperuniformity in two-dimensional, disordered, jammed packings of soft spheres”, *Physical Review E* **91**, 012302 (2015).
- ⁶³J. H. Weijs, R. Jeanneret, R. Dreyfus, and D. Bartolo, “Emergent hyperuniformity in periodically driven emulsions”, *Phys. Rev. Lett.* **115**, 108301 (2015).
- ⁶⁴A. Donev, F. H. Stillinger, and S. Torquato, “Unexpected density fluctuations in jammed disordered sphere packings”, *Physical review letters* **95**, 090604 (2005).
- ⁶⁵C. E. Zachary and S. Torquato, “Anomalous local coordination, density fluctuations, and void statistics in disordered hyperuniform many-particle ground states”, *Phys. Rev. E* **83**, 051133 (2011).
- ⁶⁶J. D. Paulsen and S. R. Nagel, “A model for approximately stretched-exponential relaxation with continuously varying stretching exponents”, *Journal of Statistical Physics* **167**, 749–762 (2017).
- ⁶⁷S. Chandrasekhar, “Stochastic problems in physics and astronomy”, *Rev. Mod. Phys.* **15**, 1–89 (1943).
- ⁶⁸J. H. Weijs and D. Bartolo, “Mixing by unstirring: hyperuniform dispersion of interacting particles upon chaotic advection”, *Physical Review Letters* **119**, 048002 (2017).
- ⁶⁹M. Florescu, S. Torquato, and P. J. Steinhardt, “Designer disordered materials with large, complete photonic band gaps”, *Proceedings of the National Academy of Sciences* **106**, 20658–20663 (2009).

- ⁷⁰W. Man, M. Florescu, E. P. Williamson, Y. He, S. R. Hashemizad, B. Y. Leung, D. R. Liner, S. Torquato, P. M. Chaikin, and P. J. Steinhardt, “Isotropic band gaps and freeform waveguides observed in hyperuniform disordered photonic solids”, *Proceedings of the National Academy of Sciences* **110**, 15886–15891 (2013).
- ⁷¹J. C. Burton, P. Y. Lu, and S. R. Nagel, “Energy loss at propagating jamming fronts in granular gas clusters”, *Phys. Rev. Lett.* **111**, 188001 (2013).
- ⁷²I. R. Peters and H. M. Jaeger, “Quasi-2d dynamic jamming in cornstarch suspensions: visualization and force measurements”, *Soft Matter* **10**, 6564–6570 (2014).
- ⁷³I. R. Peters, J. M. Amundson, R. Cassotto, M. Fahnstock, K. N. Darnell, M. Truffer, and W. W. Zhang, “Dynamic jamming of iceberg-choked fjords”, *Geophysical Research Letters* **42**, 1122–1129 (2015).
- ⁷⁴S. R. Waitukaitis and H. M. Jaeger, “Impact-activated solidification of dense suspensions via dynamic jamming fronts”, *Nature* **487**, 205–209 (2012).
- ⁷⁵M. Roché, E. Myftiu, M. C. Johnston, P. Kim, and H. A. Stone, “Dynamic fracture of nonglassy suspensions”, *Phys. Rev. Lett.* **110**, 148304 (2013).
- ⁷⁶B. Allen, B. Sokol, S. Mukhopadhyay, R. Maharjan, and E. Brown, “System-spanning dynamically jammed region in response to impact of cornstarch and water suspensions”, *Phys. Rev. E* **97**, 052603 (2018).
- ⁷⁷E. Meiburg and B. Kneller, “Turbidity currents and their deposits”, *Annual Review of Fluid Mechanics* **42**, 135–156 (2009).
- ⁷⁸T. A. Brzinski and D. J. Durian, “Observation of two branches in the hindered settling function at low reynolds number”, *Phys. Rev. Fluids* **3**, 124303 (2018).
- ⁷⁹S. R. Nagel, “Experimental soft-matter science”, *Rev. Mod. Phys.* **89**, 025002 (2017).
- ⁸⁰C. S. O’Hern, L. E. Silbert, A. J. Liu, and S. R. Nagel, “Jamming at zero temperature and zero applied stress: the epitome of disorder”, *Phys. Rev. E* **68**, 011306 (2003).

- ⁸¹W. G. Ellenbroek, E. Somfai, M. van Hecke, and W. van Saarloos, “Critical scaling in linear response of frictionless granular packings near jamming”, *Phys. Rev. Lett.* **97**, 258001 (2006).
- ⁸²P. Olsson and S. Teitel, “Critical scaling of shear viscosity at the jamming transition”, *Phys. Rev. Lett.* **99**, 178001 (2007).
- ⁸³C. J. Olson Reichhardt and C. Reichhardt, “Fluctuations, jamming, and yielding for a driven probe particle in disordered disk assemblies”, *Phys. Rev. E* **82**, 051306 (2010).
- ⁸⁴J. Wang, J. M. Schwarz, and J. D. Paulsen, “Hyperuniformity with no fine tuning in sheared sedimenting suspensions”, *Nature Communications* **9**, 2836 (2018).
- ⁸⁵L. Milz and M. Schmiedeberg, “Connecting the random organization transition and jamming within a unifying model system”, *Phys. Rev. E* **88**, 062308 (2013).
- ⁸⁶G. I. Menon and S. Ramaswamy, “Universality class of the reversible-irreversible transition in sheared suspensions”, *Phys. Rev. E* **79**, 061108 (2009).
- ⁸⁷S.-L.-Y. Xu and J. M. Schwarz, “Contact processes in crowded environments”, *Phys. Rev. E* **88**, 052130 (2013).
- ⁸⁸D. Hexner, P. M. Chaikin, and D. Levine, “Enhanced hyperuniformity from random reorganization”, *Proceedings of the National Academy of Sciences* **114**, 4294–4299 (2017).
- ⁸⁹F. Family, “Dynamic scaling and phase transitions in interface growth”, *Physica A: Statistical Mechanics and its Applications* **168**, 561–580 (1990).
- ⁹⁰D. M. Anderson, G. B. McFadden, and A. A. Wheeler, “Diffuse-interface methods in fluid mechanics”, *Annual Review of Fluid Mechanics* **30**, 139–165 (1998).
- ⁹¹J. W. Cahn and J. E. Hilliard, “Free energy of a nonuniform system. I. Interfacial free energy”, *The Journal of Chemical Physics* **28**, 258–267 (1958).

- ⁹²J. S. Huang and W. W. Webb, “Diffuse interface in a critical fluid mixture”, *The Journal of Chemical Physics* **50**, 3677–3693 (1969).
- ⁹³D. Beysens and M. Robert, “Thickness of fluid interfaces near the critical point from optical reflectivity measurements”, *The Journal of Chemical Physics* **87**, 3056–3061 (1987).
- ⁹⁴M. Kardar, G. Parisi, and Y.-C. Zhang, “Dynamic scaling of growing interfaces”, *Phys. Rev. Lett.* **56**, 889–892 (1986).
- ⁹⁵P. J. Yunker, M. A. Lohr, T. Still, A. Borodin, D. J. Durian, and A. G. Yodh, “Effects of particle shape on growth dynamics at edges of evaporating drops of colloidal suspensions”, *Phys. Rev. Lett.* **110**, 035501 (2013).
- ⁹⁶K. K. Mon, D. P. Landau, and D. Stauffer, “Interface roughening in the three-dimensional ising model”, *Phys. Rev. B* **42**, 545–547 (1990).
- ⁹⁷C. Ness and M. E. Cates, “Absorbing-state transitions in granular materials close to jamming”, *Phys. Rev. Lett.* **124**, 088004 (2020).

Vita

Jikai Wang received his B.S. degree in Physics in 2014 from University of Science and Technology of China, Anhui, China. He completed his Ph.D. degree in the Department of Physics from Syracuse University in 2021. His research interests are simulating and studying random organization in sheared suspension systems.